Fluidized bed finishing of additively manufactured objects: The influence of operating parameters

Maurizio Troiano [a,b,1], Andrea El Hassanin [a,1], Roberto Solimene [b,*], Alessia Teresa Silvestri [a], Fabrizio Scala [a,b], Antonino Squillace [a], Piero Salatino [a,b]

[a] Dipartimento di Ingegneria Chimica, Dei Materiali e della Produzione Industriale, Università degli Studi di Napoli Federico II, Piazzale V. Tecchio 80, 80125 Napoli, Italy
[b] Istituto di Scienze e Tecnologie per l'Energia e la Mobilità Sostenibili (STEMS), Consiglio Nazionale delle Ricerche (CNR), Piazzale V. Tecchio 80, 80125 Napoli, Italy

HIGHLIGHTS

- Fluidized Bed Finishing (FBF) of specimens made by additive manufacturing is investigated.
- Rotation-assisted FBF is more efficient than stationary FBF.
- Particle density is the key to the abrasive potential of powders in FBF conditions.
- Plain shear flow of abrasives close to the specimen maximizes the surface finishing.
- The finishing mechanism is associated with particle removal and plastic deformation.

GRAPHICAL ABSTRACT
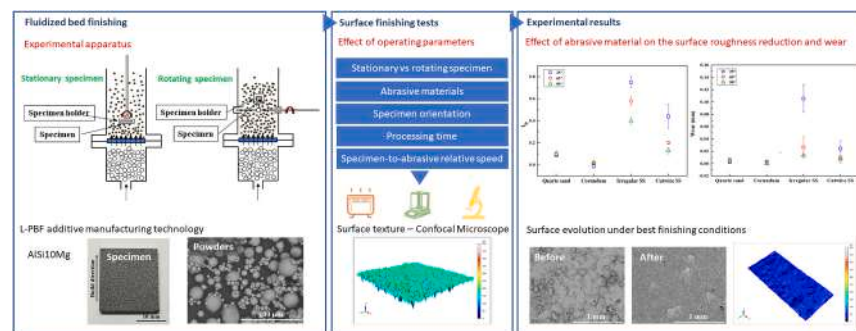
ARTICLE INFO

ABSTRACT

This study investigates the potential of Fluidized Bed Finishing (FBF) of square flat AlSi10Mg specimens manufactured via Laser-Powder Bed Fusion (L-PBF) additive manufacturing technology. Two FBF operational modes were experimentally investigated: I) with stationary specimens; II) with specimens under controlled rotational motion. Four different abrasive materials have been tested, quartz sand, corundum, irregular steel and cut wire steel particles, characterized by different hardness, density and shape. The effect of the abrasive material, processing time and specimen tilt angle was investigated. Results showed moderate smoothing under stationary specimen configuration, while good finishing for rotation-assisted tests, maximum reduction of the surface roughness of 12% and 67%, respectively. Steel particles were the most effective bed material, with particle density overtaking hardness as key particle property. The optimal tilt angle was the one that maximized sliding and shear. Altogether, surface finishing is driven by surface shear forces dominated by inertial stresses in particulate phase.

1. Introduction

Additive manufacturing (AM) technologies have experienced a hype over the last two decades, as the potential of these breakthrough manufacturing solutions have gained increasing consideration and awareness [1]. In contrast to the well consolidated manufacturing methods such as computer numerical control (CNC) machining, AM is based on the material incremental manufacturing principle, as the raw feedstock materials are consolidated into arbitrary geometries [2]. The full vision of AM covers the production of complex, composite and hybrid structures with a degree of freedom that cannot be reached by traditional manufacturing routes. Additional advantages of AM are improved resource efficiency during the production and end-use stages, longer product life and reduction of up to 80% of the lead time [3,4].

AM methods can be classified according to the nature and the aggregate state of the feedstock materials as well as by the binding mechanisms between the layers [5]. The advantages of AM based on this common manufacturing principle are particularly interesting when high added value materials are considered such as metals. Frazier reported that the leading Additive Manufacturing technologies for metals are the Laser-Powder Bed Fusion (L-PBF), Electron beam-Powder Bed Fusion (E-PBF) and Directed Energy Deposition (DED), that use powders as feedstock [6]. L-PBF technology employs a thin layer of metal powder, representing the single slice of the final part, which is 'selectively' melted through a laser, whereas the E-PBF variant is based on an electron beam as heat source. Powder-based DED is based on a different concept, as the deposition of metal powders takes place simultaneously to melting under the strong irradiance of a laser beam. In this scenario, L-PBF shares the layer-wise manufacturing principle with all AM technologies, but it represents probably the most investigated and mature AM technology for metals.

Pre- and post-processing operations are typically needed to obtain parts that meet geometrical and mechanical quality requirements. Accordingly, L-PBF (as well as most AM technologies) is not a standalone technology, but rather the core of a multi-step transformation chain including, for instance, operations aimed at controlling the powder properties [7–11], post-process heat treatments to increase parts density and to achieve the desired microstructure [12,13], post-process surface finishing to improve the surface quality [14].

The surface roughness characteristic of AM metal parts is caused by two phenomena: the stair-step effect and the balling effect [15–17]. The stair step effect occurs when inclined and curved surfaces are manufactured through the stacking of material layers of a given height, resulting in a "discretized" surface with direct detrimental effects on the surface quality. The balling effect - which is characteristic of the powder-based AM processes - occurs when, due to inappropriate choice of laser power and scanning speed, unstable melting tracks are formed, that result into overall random and sintered powder-rich surface texture. The presence of such superficial defects affects the dimensional accuracy and the mechanical, tribological and corrosion resistance of the produced parts.

Post-AM surface finishing techniques have been extensively investigated in the literature [18,19]. In the first instance, surface finishing techniques can be grouped in three categories: i) mechanical grinding and machining processes; ii) chemical and electrochemical processes, and iii) thermal energy-driven processes.

The finishing techniques belonging to group i) are mainly sandblasting [20,21], shot peening [22,23], in-situ or ex-situ CNC machining [24,25] and abrasive flow machining [26]. The grinding-based processes use abrasive particles-laden flows to perform the smoothing of the surfaces. These techniques are the most employed in the AM field, being quite effective, economically affordable, not time-consuming and environmentally friendly. CNC machining presents similar advantages, especially when realized in-situ during the part building process. However, both mechanical grinding and CNC machining techniques are characterized by a limited access of the tools to unexposed parts of complex objects, a remarkable limitation in view of the claimed design freedom characteristic of AM technology.

The capacity to treat complex geometries is a remarkable feature of group ii) finishing processes. Chemical and electrochemical polishing employs purposely formulated solutions to dissolve the material, and the physical access to unexposed parts of complex objects is accomplished by careful control of conditions of temperature, time and stirring, among the others. Electrochemical polishing is further assisted by an electric potential that helps to selectively dissolve material belonging to surface asperities rather than to the bulk and improves the control of the material removal rate [27]. These aspects make chemical-electrochemical treatments among the best candidates for the finishing of metal AM parts, as confirmed by results proposed in the literature [28–30]. Drawbacks of this method are the use of toxic substances and the possibly poor control of material dissolution when geometries, containing undercuts and solution-retaining features, are present in the object.

The finishing processes belonging to group iii) are based on smoothing mechanisms such as re-melting, ablation or a combination of the two [31] most typically induced by a laser. These processes, collectively referred to as "laser polishing", benefit from the very fine control of the energy input, high degree of automation and robustness, and may be implemented in several variants like those based on multiple different wavelengths [32–36]. Laser polishing is hampered by the limited access of the laser beam into complex features. Moreover, the thermal energy input used for the surface modification may induce residual stresses that may jeopardize the dimensional accuracy of the parts.

Several variants of the conventional processes have been investigated in an attempt to overcome their limitations. Abrasive Flow Machining (AFM) is accomplished by inducing the relative motion between an abrasive slurry and the target by means of a pneumatic system [26,37]. The motion of the abrasive slurry may be promoted by magnetic and ultrasonic fields, and its effectiveness be augmented by cavitation and chemically active media [18,38,39].

The search for novel technologies has stimulated the interest for fluidized beds of granular materials as finishing media of AM objects. Fluidization of granular solids is a well-consolidated technology, with a long record of success stories in the petroleum, power generation, process industry sectors [40]. Fluidized beds have been recently considered as surface finishing agents by turning the well-established abrasive/erosive activity of fluidized particles into a desired property. This technology, referred to as Fluidized Bed Machining (FBM), Fluidized Bed Abrasive Jet Machining (FB-AJM) or Abrasive Fluidized Bed (AFB) in previous studies, has the potential to overcome many of the drawbacks of the previously described processes, given the potential to effectively finish complex parts, the constructive simplicity of the plant, the use of harmless materials and the time- and cost-effectiveness. Barletta and co-workers pioneered this technology by investigating the finishing of wrought aluminum sheets and complex geometry parts, assessing the effects of process variables such as time, abrasive characteristics and related impact speed, roughness of the substrate on the surface quality evolution and wear [41]. The potential of FBF was eventually investigated for the surface treatment of aluminum tubes [42], Inconel 718 [43], and PVC parts [44–46]. Atzeni et al. [47–50] investigated the finishing of additive manufactured substrates in fluidized beds and their fatigue behaviour after fluidized bed treatment, for different operating conditions and different materials (AlSi10Mg, Ti6Al4V, Co-Cr parts). Kim and Lee recently reported a simulation and experimental analysis of FBF of stainless steel 304 substrates [51]. El Hassanin et al. [52,53] and Troiano et al. [54] investigated FBF of AlSi10Mg parts produced by L-PBF by dipping square flat specimens into a bubbling fluidized bed and analyzed the effect of different abrasive materials and positioning of the samples. El Hassanin et al. [55] recently reported preliminary results on the effect of rotational motion of specimens in fluidized beds. FBF has also been considered in combination

with the use of chemically aggressive solutions [56], although the potential of the integrated process might be questioned because of the additional complexity it brings about. Altogether, FBF assisted by the relative motion between the fluidized suspension and the specimen stems out as a promising path toward an effective, manageable, and environmentally friendly solution, and will be the specific focus of this study.

Modelling surface finishing of metal objects in fluidized beds must consider the detailed micromechanics of the interaction between the object and the granular suspension. Much inspiration has been taken in the past from the neighboring field of erosion of objects immersed in fluidized beds. However, there is a fundamental argument when mathematical and phenomenological models of FBF are borrowed from the field of erosion of internals in fluidized beds. This is a case where smooth surfaces are exposed to the damage from moving particles. On the contrary, FBF entails the smoothing out of a rough surface by the fluidized suspension. The implication of this fundamental difference will be discussed in the present study when analyzing results of an experimental campaign on FBF treatment of AlSi10Mg alloy specimens manufactured by L-PBF. The effect of the operational mode has been assessed by comparing results from experiments with stationary specimens with those from experiments where relative motion between the bed and the specimen was established by imparting rotational motion to the object. The effect of operating conditions, namely bed materials, tilt angle, and duration of the finishing test, has been assessed. Analysis of results is directed to shed light on mechanisms relevant to surface finishing.

2. Materials and methods

2.1. L-PBF specimens and abrasive materials

The experiments reported in this study were performed using square flat specimens (dimensions: $20 \times 20 \times 2$ mm^3), built perpendicularly to the building platform during the L-PBF process. The samples were manufactured using an EOS EOSINT M280 L-PBF (no longer commercially available) machine starting from AlSi10Mg powders provided by EOS GmbH. The particle size of the AlSi10Mg powders, whose chemical composition is reported in Table 1, was determined according to the ASTM B822 standard [57] and ranged between 13 and 57 μm with the following percentiles: d10 = 13.5 μm; d50 = 31.2 μm; d90 = 56.8 μm. An image of a typical specimen used for the experiments and a SEM image of the powders used for the L-PBF process are reported in Fig. 1. Concerning the L-PBF powder feedstock, the SEM image reported in Fig. 1 shows the presence of smaller satellite particles surrounding the bigger ones: this phenomenon is very common in the gas-atomization process and due to the impact of the particles upon solidification and cooling [58]. The process parameters used to build the specimens were chosen according to the *EOS Part Property Profile AlSi10Mg Speed 30* μm guidelines, provided by EOS GmbH. More specifically, the printing parameters were the following: laser power P = 370 W, hatch spacing h = 0.19 mm, scanning speed v = 1300 mm/s and layer thickness L_T = 30 μm. The set of process parameters resulted in a volumetric energy density VED_h = 49.9 J/mm^3. Each layer of the build was obtained using a raster scanning strategy and adopting a rotation angle of 67° between consecutive layers to optimize the thermal input distribution during the process and no contouring was performed. Subsequently, the samples were stress relieved by heat treatment at 300°C for 2 h. As a result, the average Vickers microhardness of the as-built samples, measured along their building direction, was approximately 90 HV. The building strategy and the parameters used in the manufacturing process are such that

the stair-case effect is fairly negligible in the final specimens, while balling effect and the presence of sintered particles are likely to be the main phenomena that negatively affect the surface quality characteristics.

Four abrasive materials were selected to investigate the effect of material properties on the FBF process. Table 2 and Table 3 report the main properties of the selected bed materials in terms of chemical composition, density, size, hardness, and shape. Corundum and quartz sand particles were chosen in view of their large hardness, whereas steel (SS) particles were chosen to explore the effect of high-density abrasives on the surface smoothing efficiency. For the latter type of abrasive material, the particles shape was also considered as a process variable to evaluate the effect of their morphology on the interactions with the impinged surface. Particle size distribution was determined using a laser diffraction analyzer (Malvern Mastersizer 2000). In Tables 2 and 3, the mean size corresponds to the Sauter mean diameter. Furthermore, the percentiles values d10, d50 and d90 are also reported for all the investigated materials.

2.2. Fluidized bed finishing (FBF)

2.2.1. Experimental apparatus

2.2.1.1. Experiments with stationary specimen. FBF experiments were carried out with the apparatus illustrated in Fig. 2, also described elsewhere [52,53]. The experimental setup consisted of a Plexiglas fluidization column (inner diameter 0.21 m) which comprises a ceramic rings-filled windbox and an upper section, 1.4 m high, where the abrasive material was located. The fluidizing gas, technical air, was fed at the bottom of the windbox and flowed through a steel bubble caps plate acting as gas distributor to the fluidization section of the column. The carrier gas was controlled by a mass flow meter (*Bronkhorst EL-Flow Select*) with a maximum operating flow rate of 200 Nm^3/h (corresponding to a superficial gas velocity available up to 1.6 m/s). Each experiment was carried out using a purposely made sample holder, mounted on a vertical threaded bar that allowed the insertion of the specimen from the top of the column at a fixed height of 150 mm from the gas distributor. A scheme of the fixture with the positioning of the specimen is reported in Fig. 2a. The specimen holder could be also tilted, as illustrated in Fig. 2b, to investigate the effect of the relative inclination of the specimen with respect to the vertical direction, i.e. the preferential direction of the impinging abrasives. In particular, when the target was orthogonal to the threaded bar (axial direction of the fluidization column) it was considered that the inclination (tilt angle) of the target, α, was equal to 0°; when the target was parallel to the vertical threaded bar, α = 90°. Taking into account that during fluidization the bed material preferentially moves along the axial direction of the fluidization column, for these two limit inclinations of the target (α = 0° and α = 90°) normal and glancing impacts are obtained [59] respectively (particles/target impact angle θ = 90° and 0°, respectively).

2.2.1.2. Rotation-assisted FBF experiments. The experimental setup used for the FBF experiments is reported in Fig. 3. It consisted of the same Plexiglas fluidization column described for the stationary specimen experiments. For these experiments, the purposely made specimen holder was mounted on a rotating horizontal shaft and connected to an electrical motor. The specimen was inserted from the top of the lower column section at a height of 150 mm from the metal bubble caps

Table 1
Chemical composition of the AlSi10Mg SLM powders feedstock.

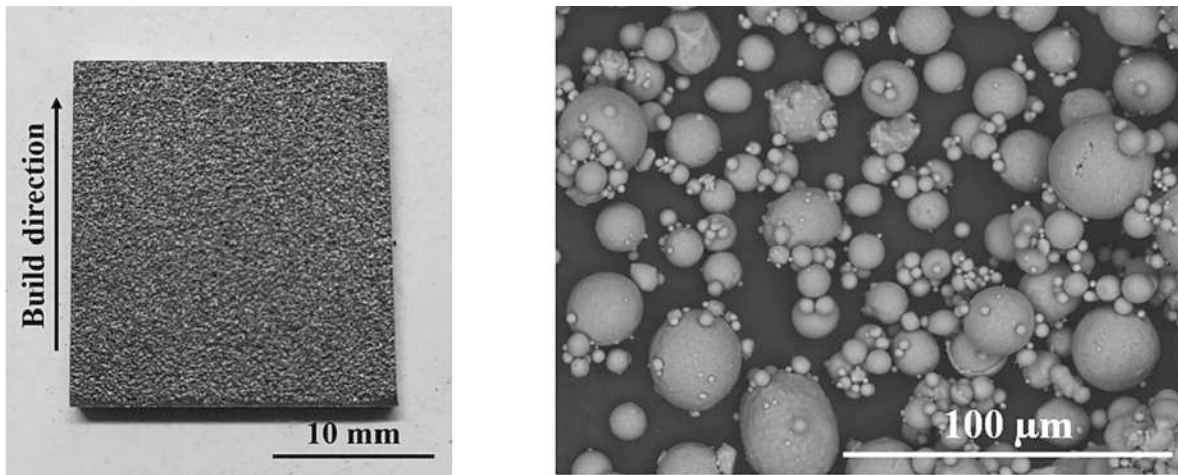| Element	Al	Si	Fe	Cu	Mn	Mg	Ni	Zn	Pb	Sn	Ti
wt%	balance	9.0–11.0	<0.55	<0.05	0.45	0.2–0.45	<0.05	<0.10	<0.05	<0.05	<0.15

Fig. 1. (a) L-PBF specimen used for the experiments and (b) SEM image of the AlSi10Mg powders used for the L-PBF process (magnification 1000×).

Table 2
Silica sand and alumina particles properties.

Abrasive	Chemical composition (%wt)				Particle Density $\left(\frac{kg}{m^3}\right)$	Hardness (HV)	Mean size (µm)	d10	d50	d90	Shape
	Al_2O_3	Fe_2O_3	SiO_2	TiO_2					(µm)		
Quartz sand	–	–	–	–	2570	900	603	439	623	905	Irregular
Corundum	Bal.	0.035	0.023	0.006	3870	2300	511	347	540	845	Irregular

Table 3
Irregular and Cut wire steel (SS) particles properties.

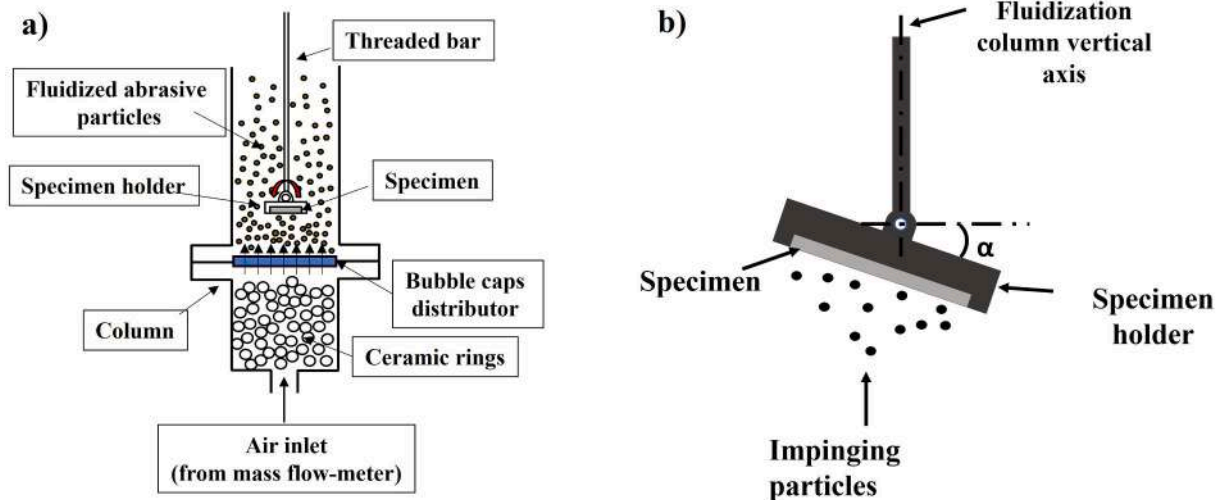| Abrasive	Chemical composition (%wt)				Particle Density $\left(\frac{kg}{m^3}\right)$	Hardness (HV)	Mean size (µm)	d10	d50	d90	Shape
	Fe	C	Si	Mn					(µm)		
Irregular SS	Bal.	0.8	0.4	0.35	7600	500	529	330	574	1037	Irregular
Cut wire SS	Bal.	0.55	0.2	0.5	7600	480	500	380	512	690	Cylindrical

Fig. 2. Scheme of the experimental apparatus used for the FBF experiments with stationary specimen (a) with an inset of specimen positioning and tilt angle (b).

distributor. The rotation of the clamping system was provided by means of an electrical motor regulated by an inverter. The horizontal rotation of the sample was chosen as it has been already adopted in other experimental facilities for rotation-assisted FBF [47] and, thus, it allows for the comparison of the experimental results. A scheme of the experimental apparatus with the positioning of the specimen is reported in Fig. 3a. A CAD scheme of the specimen holder with the specimen positioning and the tilt angle is illustrated in Fig. 3b. In particular, when the specimen plane was orthogonal to the rod of the specimen holder it is considered that the inclination (tilt angle) of the target, α, is equal to 0°,
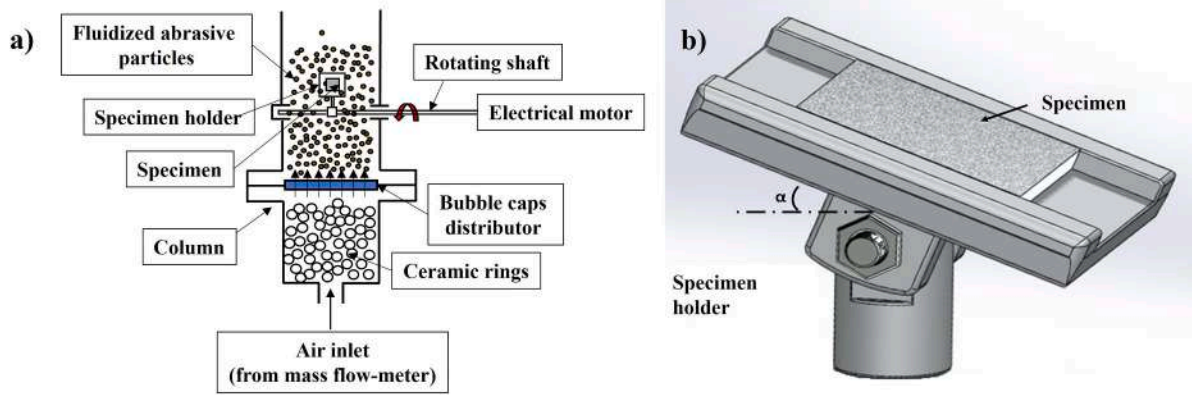
Fig. 3. Scheme of the experimental apparatus used for the rotation-assisted FBF experiments (a) with an inset of specimen positioning and tilt angle (b).

whereas when the specimen plane is parallel to the rod of the specimen holder, $\alpha = 90°$.

2.2.2. Experimental procedure

2.2.2.1. Experiments with stationary specimen. The experiments were carried out to investigate the effect of the abrasive materials, finishing time and target inclination on the finishing process during FBF. The operating conditions and process parameters used in the experimental campaign are reported in Table 4. In particular, three target tilt angles α were chosen to investigate, for each abrasive material, the two possible extreme positions of the sample surface (0°, 90°) as well as the specific value of 25° that, according to literature, maximizes all the surface-abrasive interaction mechanisms in FBF [44]. The experiments were carried out under bubbling fluidization regime for a specified value of the excess of the fluidization velocity with respect to the velocity at incipient fluidization, U-$U_{mf} = 0.8$ m/s and not at the same fluidization velocity. This choice allows to compare the FBF obtained with the different investigated materials at similar bubbling fluidization conditions but not at the same operation costs which depends on the fluidization velocity. The incipient fluidization velocity U_{mf} for each bed material was experimentally determined and is reported in Table 4 together with the superficial gas velocity used during the experiments for each abrasive material. A total finishing time of 90 min was set for each experiment, evaluating the effects of the finishing treatment at time-steps of 30 min. The reproducibility of the results was assessed by repeating each experiment three times.

2.2.2.2. Rotation-assisted FBF experiments. In this case, the experiments were carried out to investigate the effect of the abrasive materials, rotation speed (*v*) and target inclination (*α*) on the finishing process during the rotation-assisted FBF tests. The bed was operated under incipient fluidization conditions and the processing time was fixed at 30 min for each test. The operating conditions and process parameters used in the experimental campaign are reported in Table 5. In particular, three target tilt angles *α* were chosen for each abrasive material, equal to

Table 4
Process parameters and operating conditions of FBF experiments.

Process time (min)	Tilt angle α (°)	U_{mf} (m/s)				U-U_{mf} (m/s)
		Quartz sand	Corundum	Irregular SS	Cut wire SS	
30	0					
60	25	0.2	0.42	0.47		0.8
90	90					

Table 5
Process parameters and operating conditions used of rotation-assisted FBF experiments.

Abrasive	Tilt angle α (°)	Average tangential velocity (m/s)	Process time (min)
All	25	1±0.09 2±0.18	30
	65	1±0.25 2±0.5	
	90	1±0.3 2±0.6	

25, 65 and 90°. The relative velocity between the fluidized abrasive bed and the sample has been assumed equal to the average tangential speed of the sample, as under minimum fluidization conditions the velocity of fluidized particles can be neglected. Moreover, the tangential speed is a function of the punctual distance of the sample from the rotation axis as well as of the sample tilt angle. Two values of tangential velocity *v* were considered, i.e. 1 and 2 m/s, averaged over the specimen based on the knowledge of the distance from the rotation axis, the rotation speed and the tilt angle.

2.2.3. Characterization of the specimens

Before and after each treatment step, the specimens were accurately cleaned by means of an ultrasonic bath in ethanol for 15 min, followed by air blowing and drying at 80°C for 1 h. Subsequently, the surface modifications after the treatment were quantified through a Leica DCM3D Confocal Microscope. For each acquisition, an 8×8 mm^2 area was considered, taking the sample center as a reference point. The acquired surfaces were then post-processed to correct tilt errors, to fill the missing points and to extract the surface texture parameters by means of the software Leica Map® v7. Given the random texture of SLM produced parts, no filtering was performed during the surface analysis. Two areal parameters were investigated, i.e. the mean areal surface roughness S_a and the areal skewness S_{sk}, to describe the surface modifications after FBF and to compare the results with the as-built surface condition [60]. The roughness parameter S_a represents the areal equivalent of the most widespread mean profile roughness R_a, whereas the skewness parameter S_{sk} describes the distribution symmetry of peaks and valleys within the acquired area, in this case mainly represented by the partially molten powders on the surface. The resulting values were expressed in terms of mean and standard deviation, resulting from the repeated experiments related to the specific set of process parameters. Furthermore, the root mean square of the primary profile slope, P_{dq}, was considered [61]. According to some experiments reported in literature [62], this parameter, which represents the actual slope of a primary profile acquired from a surface, can be related to the smoothness and brilliance of

a surface. Moreover, in the case of surface treatments of metal powder-based AM parts, P_{dq} could represent a further useful indicator of the smoothing mechanisms in relation to the specific surface texture investigated for the as-built samples. On the other hand, the equivalent areal parameter, S_{dq}, was not investigated since it describes a surface gradient that provides a less clear information on the entity of the treatment-induced modifications [60]. The evolution of P_{dq} was investigated by considering the mean and standard deviation over ten profiles — five for each of the two orthogonal directions identifying the sample area — extracted from the acquired surface by means of procedures available in Leica Map® v7. The quantitative analysis was also compared with the observation of the surface morphology evolution by means of SEM imaging before and after each treatment step, using a Hitachi TM3000 SEM. Finally, measurement of the specimen mass was performed to estimate the cumulative percentage weight loss and the wear of the samples.

3. Results and discussion

3.1. FBF of stationary specimens

The evolution of the surface texture parameters and the cumulative fractional weight loss are reported in Table 5 for quartz sand and corundum abrasives and in Table 6 for the irregular and cut wire SS abrasives. The first remarkable result is the fairly broad dispersion of the surface texture parameters, namely S_a, S_{sk}, and P_{dq}, of the raw untreated specimens, as evident from the analysis of the time 0 column for each material in the Tables 6 and 7. This result can be ascribed to the random nature of as-built L-PBF surfaces. It is noteworthy that the surface defects of the samples in this study are mainly related to the presence of a layer of partially molten alloy powders due to the balling effect [15]. Since no build angles were established during the L-PBF manufacturing process, the stair-step effect was absent. The surface texture properties in Tables 6 and 7 highlight that the FBF was moderately active for most of the investigated operating conditions and for all the investigated abrasive powders. The improvements of surface quality are more appreciable as the tilt angle and the finishing time increased.

Regardless of the abrasive material, the 90° tilt angle (tangential flow of abrasive particles) promoted the best finishing performance. In Tables 6 and 7 it is evident that, at fixed inclination of the target, all the surface texture features decreased and the cumulative weight loss increases with finishing time. As an example, for a tilt angle of 90°, the largest S_a reduction was observed for the SS abrasive powders: a roughness reduction of 2 μm was achieved from a starting value of 20.4 μm for the irregular SS abrasive, whereas for the cut wire SS abrasive S_a was reduced of approximately 3 μm from an initial roughness of 24.6 μm. On the other hand, the results obtained from the use of quartz sand and corundum abrasives showed that the FBF effect on the tested samples was even lower and less appreciable, with the highest S_a reduction of 1.6 μm and 0.9 μm respectively after 90 min of treatment.

Surface finishing of stationary specimens turns out to be fairly slow, with the possible exception of experiments performed with cut wire SS abrasive where a decrease of the roughness was noticeable after 30 min finishing. Analysis of the symmetry parameter S_{sk} leads to similar conclusions. Untreated specimens exhibit variable S_{sk}, with a large dominance of negative values which suggests the prevalence of pits or valleys over spikes and crests. An appreciable reduction of S_{sk} after finishing was observed only for the irregular SS case, with a variation of -0.2 from the mean starting value of -0.2, whereas the adoption of the other abrasives did not significantly influence this parameter. On the other hand, the P_{dq} evolution reported in Tables 6 and 7 showed a higher sensitivity for all the abrasives, except corundum, and tilt angles. Furthermore, a dependency of this parameter from the process time was observed for the SS and quartz sand abrasives. As reported in Tables 6 and 7, the cumulative fractional weight loss increases with finishing time, approaching values as large as 0.3% after 90 min for the cut wire SS abrasive (90°) and for quartz sand and corundum powders (25°).

Considering the significant differences of the random surface texture of the manufactured samples before the treatment, the more general experimental outcome is that the main surface modifications induced by the investigated FBF process conditions were the partial removal of the sintered metal powders on the surface. This outcome was more clearly observed from the comparison between the SEM images of the surfaces before and after the treatment (90 min), reported in Fig. 4 as a function

Table 6

Surface texture parameters and cumulative fractional weight loss obtained from the FBF experiments with quartz sand and corundum abrasives (results are reported as mean ± σ).

		Quartz sand				Corundum			
		Time (min)				Time (min)			
	Tilt angle α (°)	0	30	60	90	0	30	60	90
S_a (μm)	0	22.8 ±2.0	21.9 ±1.4	21.5 ±1.4	21.2 ±1.7	20.1 ±0.2	19.5 ±0.2	19.5 ±0.3	19.4 ±0.4
	25	21.1 ±1.2	20.3 ±1.0	20.2 ±0.7	19.7 ±1.1	20.3 ±0.7	19.7 ±0.4	19.6 ±0.2	19.6 ±0.2
	90	22.0 ±0.8	21.4 ±1.0	20.9 ±1.1	20.4 ±0.7	20.4 ±0.6	19.7 ±0.4	19.7 ±0.3	19.5 ±0.4
S_{sk}	0	−0.1 ±0.2	−0.1 ±0.2	−0.2 ±0.2	−0.2 ±0.2	−0.3 ±0.4	−0.3 ±0.3	−0.3 ±0.4	−0.3 ±0.4
	25	−0.3 ±0.2	−0.3 ±0.3	−0.4 ±0.3	−0.4 ±0.2	−0.3 ±0.2	−0.2 ±0.3	−0.3 ±0.3	−0.3 ±0.3
	90	−0.1 ±0.2	−0.1 ±0.3	−0.1 ±0.3	−0.1 ±0.3	−0.4 ±0.1	−0.3 ±0.2	−0.3 ±0.2	−0.4 ±0.1
P_{dq} (°)	0	53 ±9.0	45 ±9.0	42 ±12.0	35 ±3.0	43 ±4.0	38 ±4.0	37 ±3.0	35 ±4.0
	25	52 ±9.0	43 ± 3.0	41 ±6.0	35 ±2.0	45 ±7.0	36 ±5.0	33 ±6.0	30 ±2.0
	90	56 ±2.0	43 ±7.0	38 ±8.0	34 ±6.0	39 ±4.0	35 ±2.0	34 ±3.0	34 ±2.0
Cumulative weight loss (%)	0	–	0.139 ± 0.06	0.231 ± 0.04	0.278 ± 0.03	–	0.098 ± 0.04	0.197 ± 0.04	0.197 ± 0.03
	25	–	0.152 ± 0.04	0.253 ± 0.04	0.304 ± 0.03	–	0.098 ± 0.05	0.196 ± 0.03	0.294 ± 0.03
	90	–	0.142 ± 0.04	0.189 ± 0.02	0.236 ± 0.02	–	0.063 ± 0.05	0.125 ± 0.04	0.154 ± 0.04

Table 7
Surface texture parameters and cumulative fractional weight loss obtained from the FBF experiments with irregular and cut wire steel (SS) abrasives (results are reported as mean $\pm$ σ).

|		Irregular SS				Cut wire SS			
		Time (min)				Time (min)			
	Tilt angle α (°)	0	30	60	90	0	30	60	90
S_a (μm)	0	21.4 ±2.9	20.9 ±2.8	20.7 ±2.8	20.4 ±2.7	21.3 ±1.9	20.5 ±1.4	20.2 ±1.4	20.2 ±1.2
	25	21.0 ±1.6	20.4 ±1.7	20.2 ±1.7	20.1 ±1.7	23.3 ±0.7	22.3 ±0.8	22.2 ±0.7	22.0 ±0.7
	90	20.4 ±1.4	19.3 ±1.5	18.7 ±1.4	18.4 ±1.4	24.6 ±0.6	23.1 ±0.0	22.4 ±0.2	21.9 ±0.1
S_{sk}	0	−0.2 ±0.4	−0.3 ±0.3	−0.4 ±0.4	−0.4 ±0.3	−0.1 ±0.2	0.0 0 ± 0.3	0.0 ±0.3	0.0 ±0.3
	25	−0.1 ±0.2	−0.2 ±0.2	−0.2 ±0.2	−0.3 ±0.2	0.0 ±0.1	0.0 ±0.1	0.0 ±0.1	−0.1 ±0.1
	90	−0.1 ±0.1	−0. 2 ± 0.1	−00 .3 ± 0.2	−0.4 ±0.2	0.0 ±0.3	0.0 ±0.3	0.0 ±0.2	−0.1 ±0.2
P_{dq} (°)	0	52 ±4.0	45 ±3.0	39 ±3.0	29 ±2.0	50 ±10.0	33 ±5.0	32 ±5.0	32 ±3.0
	25	55 ±3.0	49 ±5.0	43 ±9.0	31 ±6.0	47 ±9.0	38 ±4.0	36 ±3.0	36 ±3.0
	90	53 ±4.0	49 ±3.0	43 ±4.0	27 ±1.0	47 ±5.0	35 ±2.0	35 ±2.0	34 ±3.0
Cumulative weight loss (%)	0	–	0.036 ± 0.05	0.052 ± 0.03	0.056 ± 0.03	–	0.012 ± 0.04	0.043 ± 0.03	0.038 ± 0.03
	25	–	0.049 ± 0.06	0.102 ± 0.04	0.115 ± 0.04	–	0.165 ± 0.06	0.230 ± 0.06	0.229 ± 0.05
	90	–	0.048 ± 0.05	0.092 ± 0.05	0.118 ± 0.03	–	0.210 ± 0.07	0.294 ± 0.04	0.345 ± 0.04
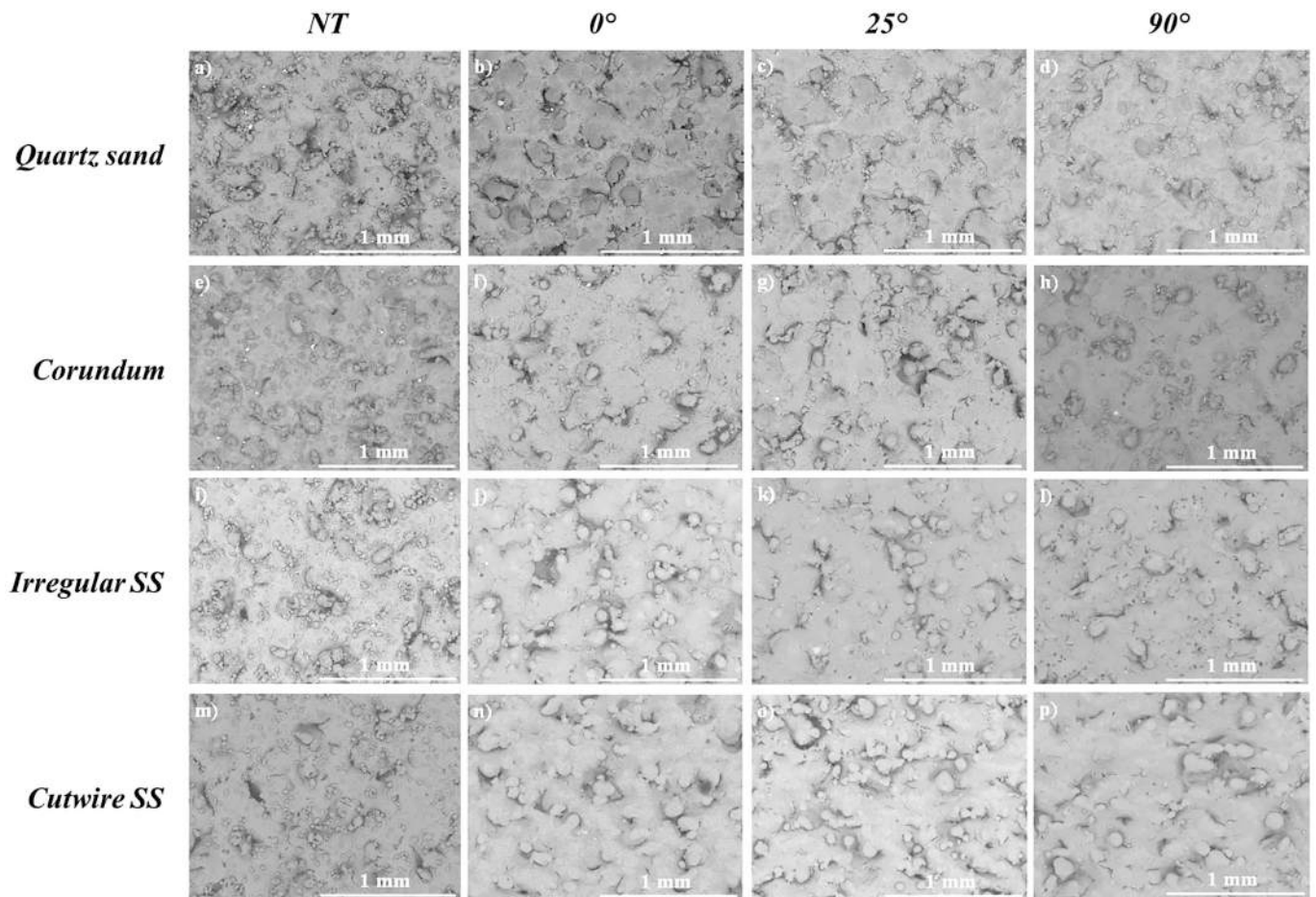
Fig. 4. SEM images before and after the treatment (90 min), as a function of the abrasive materials and the specimen tilt angle α (100× magnification).

of the tilt angle and the nature of the abrasive powder. The images also showed the presence of defects such as craters and undercuts on the as-built surfaces (Fig. 4a to m), most likely due to typical L-PBF drawbacks such as the lack of fusion and the balling effect [16]. As a result, a stable and precise definition of the surface quality status for the as-built samples was difficult to achieve.

Altogether, results indicate that finishing of stationary specimens brings about only modest improvements of the surface quality. This finding is attributed to the limited extent of mechanical energy associated with shear and/or impact which could be converted into deformation/removal of the superficial defects. Despite the poor performance of FBF with stationary specimens, an important outcome of this experimental campaign was the assessment of the influence of the nature of the abrasive material and of the tilt angle on the mechanisms of surface finishing. To better appreciate these effects, the fractional change I_{fp} of the mean areal surface roughness S_a, defined as:

$$I_{fp}(t) = \frac{S_a^0 - S_a(t)}{S_a^0}$$

has been introduced and calculated for all the finishing conditions. This indicator varies between 0, when the surface finishing process is totally ineffective, and 1, when the mean areal surface roughness S_a vanishes. It is recalled that S_a is measured on an area of 8×8 mm^2 corresponding to the central part of the sample. The extension of the investigated area is such that S_a, even in presence of disuniformities of the finishing

treatment, can give, as a first-order approximation, a representative estimation of mean roughness of the entire specimen surface. Fig. 5 reports the temporal evolution of this indicator for all the abrasive particles and for the different tilt angles investigated.

The analysis of data in Fig. 5 highlights that:

1) The nature of abrasive powders seems to barely influence the surface finishing for low values of α. I_{fp} is similar for all the investigated materials for α equal to 0° and 25° for given finishing time.
2) The influence of the nature of abrasive powder is remarkable at α = 90°. I_{fp} values are higher for powders characterized by higher density (SS abrasives) rather than those by higher hardness (quartz sand, corundum) whatever the particle shape and finishing time. Besides, values of I_{fp} for the irregular and cutwire SS abrasives are very similar. Thus, for this condition, it is evident that the hardness of the abrasive material and the particle shape do not play a major role, whereas the density of the material seems to be crucial in determining the performance of the surface finishing process.
3) The best surface finishing performance is obtained for α = 90° for the denser SS abrasive particles. This means that parallel shear flow of the granular phase over the specimen is more effective to surface finishing than orthogonal flow [63]. The remarkable effect of particle density suggests that inertial forces in the dense granular phase might play a key role in the momentum exchange between the fluidized bed and the specimen [63,64].
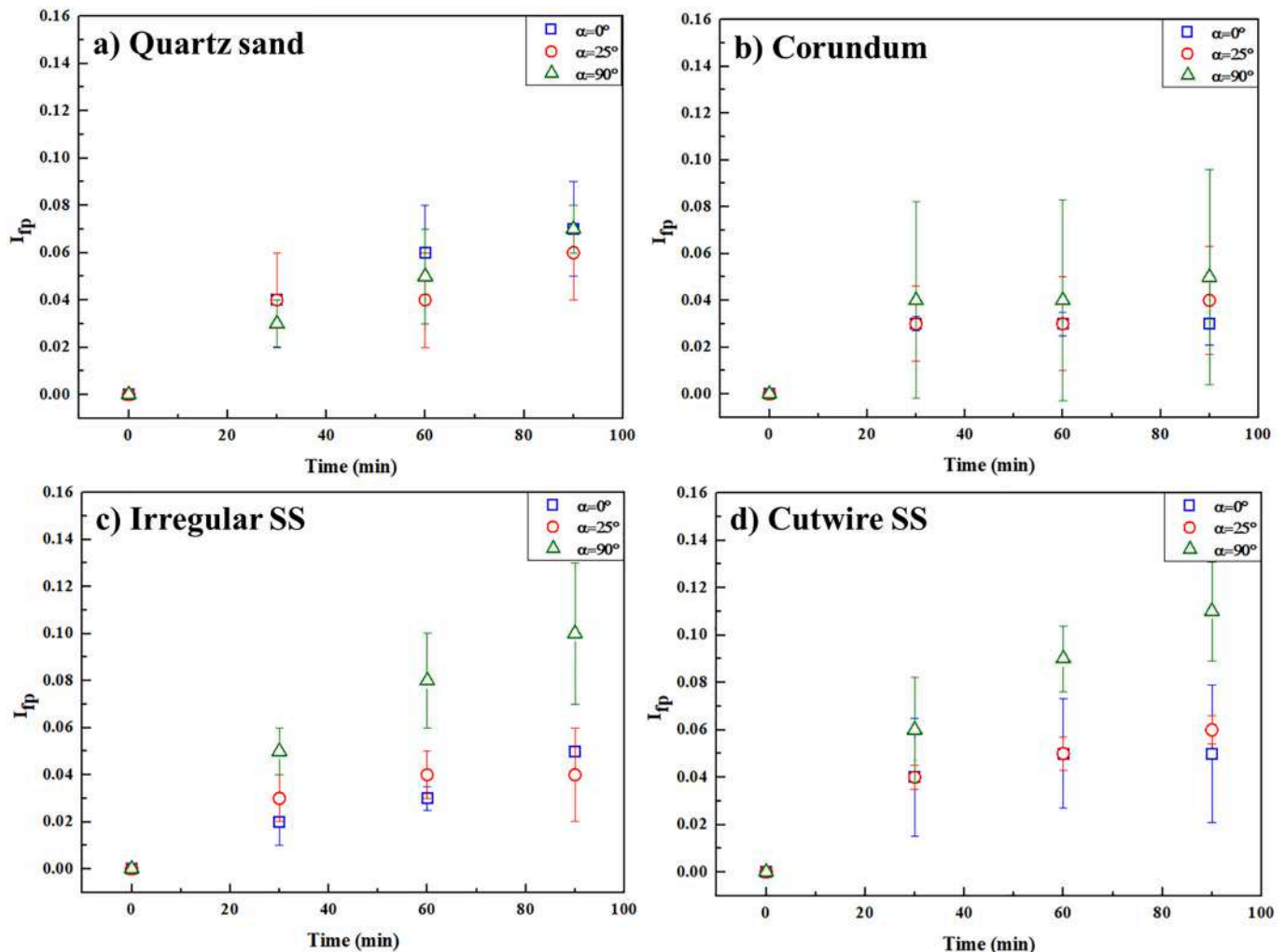

Fig. 5. Time-resolved profile of surface finishing parameter I_{fp} for the four tested abrasive materials varying the tilt angle α (error bars indicate a deviation of ±σ).

It is remarkable that the optimum tilt angle of 25° experimentally determined in previous studies [44] for the FBF of sintered parts is not confirmed under the experimental conditions used in the present study.

The experimental data were further elaborated to calculate the wear of the sample over the finishing time while varying the impact angle and the abrasive material. The wear was calculated as the ratio between the removed mass and the average area of the target according to:

$$wear = \frac{W^0 - W(t)}{\rho_s A_s}$$

where W^0 and $W(t)$ are the initial mass and the mass at finishing time t of the specimen, and ρ_s, and A_s are the density and the exposed surface of the sample, respectively. The wear represents the thickness of a layer of material uniformly removed throughout the entire specimen surface. The temporal evolution of the wear is reported in Fig. 6.

The analysis of the data reported in Fig. 6 highlights that:

- The tilt angle barely influences wear for quartz sand, corundum and irregular steel particles, whereas it plays a significant role for the cutwire abrasive particles.
- The wear for the harder materials, i.e. quartz sand and corundum particles, is larger than that observed for the irregular SS material and similar to that of cutwire abrasive for tilt angle equal to zero.
- The wear increases less than linearly with the finishing time.

Comparison of the trends of specimen wear and of the surface finishing parameter I_{fp} suggests that surface finishing is only partially correlated to wear. The harder quartz sand and corundum particles lead to larger material removal of the target surface, but this is not reflected by better surface finishing. It is likely that wear for hard materials is mostly related to removal of fine particles remaining on the surface by the AM process, without appreciable modifications of the key morphological surface features in terms of peaks and pits/valleys, so that the superficial roughness is left substantially unchanged. Instead, the less pronounced wear associated with irregular SS abrasive together with the best performance in terms of S_a roughness indicate that the mechanisms active for the surface finishing with this abrasive is a combination of particle removal due to wear combined with plastic deformation of sample surface induced by the action of shear stress of the fluidized solid phase.

3.2. Rotation-assisted FBF experiments

3.2.1. Experiments with rotational speed v = 1 m/s

The values of the surface texture parameters of the specimens before and after FBF are reported in Table 8. The much larger effectiveness of rotation-assisted FBF compared with FBF of stationary specimens is remarkable. The most effective abrasive material was again represented by SS, and in particular by irregular SS particles that give rise to the more extensive surface roughness reduction and specimen weight loss.
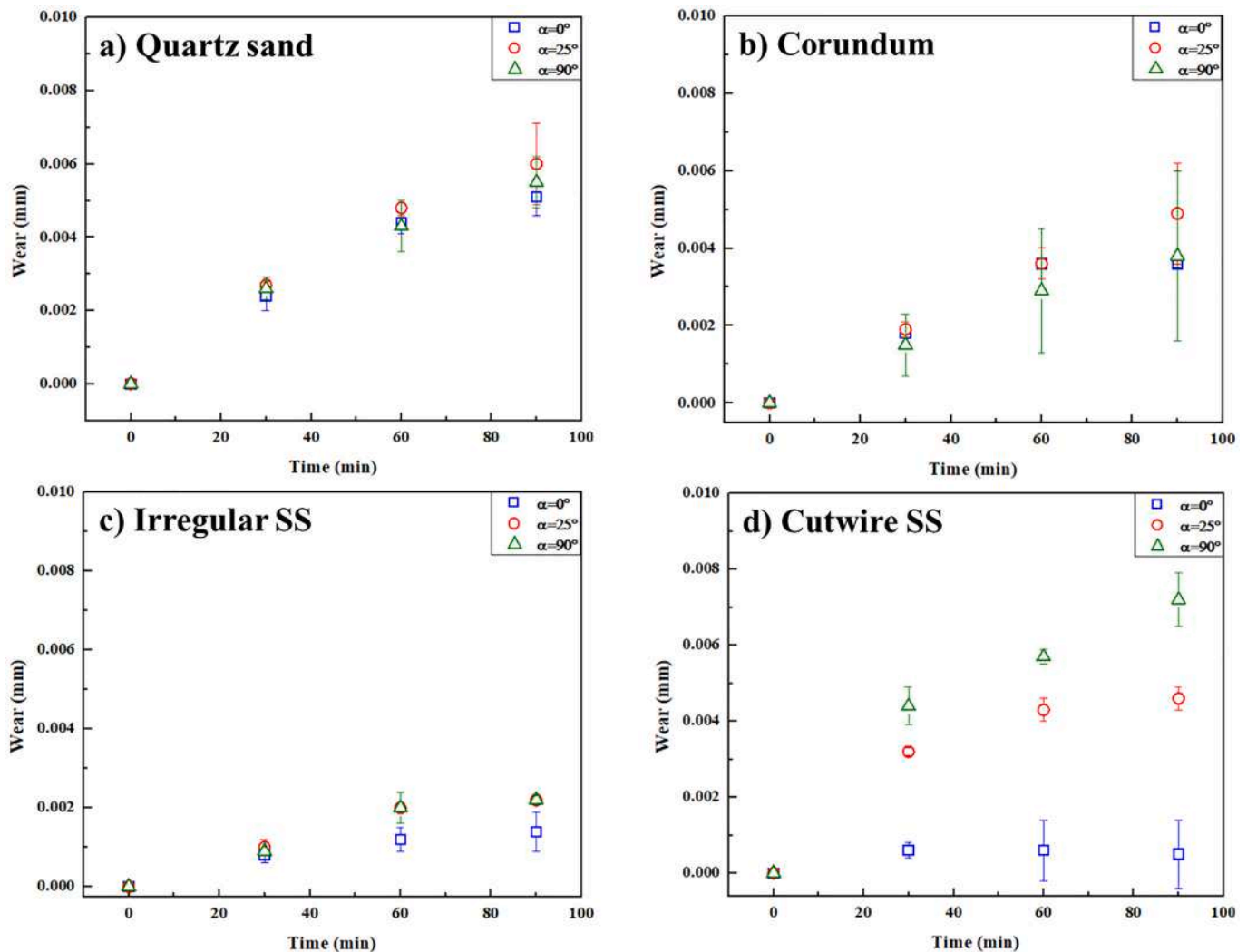

Fig. 6. Time-resolved profile of wear for the four tested abrasive materials varying the tilt angle α (error bars indicate a deviation of ±σ).

Table 8
Surface texture parameters of specimens for rotation-assisted FBF at $v = 1$ m/s (results are reported as mean ± σ).

	Tilt angle α (°)	Quartz sand		Corundum		Irregular SS		Cutwire SS	
		NT	30 min	NT	30 min	NT	30 min	NT	30 min
S_a (μm)	25	22.8 ±0.4	22.1 ±0.7	20.7 ±2.1	18.9 ±0.5	21.5 ±3.3	16.9 ±2.7	21.9 ±2.4	20.3 ±1.8
	65	23 ±1.8	21 ±2.3	21.1 ±1	20.8 ±1	21.4 ±2.8	16.3 ±0.3	24.7 ±0.5	22.2 ±0.2
	90	23.1 ±0.5	21.3 ±0.8	19.8 ±0.5	19.6 ±0.5	20 ±0.1	19.2 ±1	23.9 ±0.8	21.9 ±1.1
S_{sk}	25	0.03 ±0.08	−0.04 ±0.08	−0.04 ±0.14	−0.06 ±0.15	0.04 ±0.06	−0.84 ±0.43	−0.02 ±0.28	−0.02 ±0.43
	65	−0.02 ±0.05	−0.04 ±0.24	−0.40 ±0.14	−0.40 ±0.14	−0.02 ±0.5	−0.96 ±0.06	0.02 ±0.17	0.14 ±0.19
	90	0.18 ±0.05	0.05 ±0.23	−0.27 ±0.09	−0.37 ±0.1	−0.27 ±0.23	−0.5 ±0.27	0.18 ±0.04	0.31 ±0.01
P_{dq} (°)	25	43 ±2.5	35 ±2.1	36 ±3.2	32 ±2.7	37 ±3.4	26 ±3.5	37 ±2.7	33 ±3.6
	65	40 ±4.1	33 ±3.4	35 ±4.0	32 ±4.2	35 ±3.3	23 ±4.0	41 ±3.6	36 ±3.3
	90	43 ±4.1	34 ±3.1	33 ±4.5	32 ±3.4	31 ±3.6	30 ±3.9	43 ±3.4	39 ±3.6
Cumulative Weight loss (%)	25	–	0.144 ± 0.1	–	0.027 ± 0.03	–	0.441 ± 0.25	–	0.305 ± 0.18
	65	–	0.241 ± 0.05	–	0.000 ± 0.00	–	0.359 ± 0.18	–	0.239 ± 0.1
	90	–	0.144 ± 0.01	–	0.049 ± 0.01	–	0.157 ± 0.008	–	0.767 ± 0.05

This result confirms the expectation that a much more extensive momentum and energy transfer between the bed and the specimen is achieved when a relative motion is established between the specimen and the bed. Results for different tilt angles indicate that surface finishing is at its best for α = 25°, although comparable results were obtained for the 65° value. It is noteworthy that, for this experimental configuration,
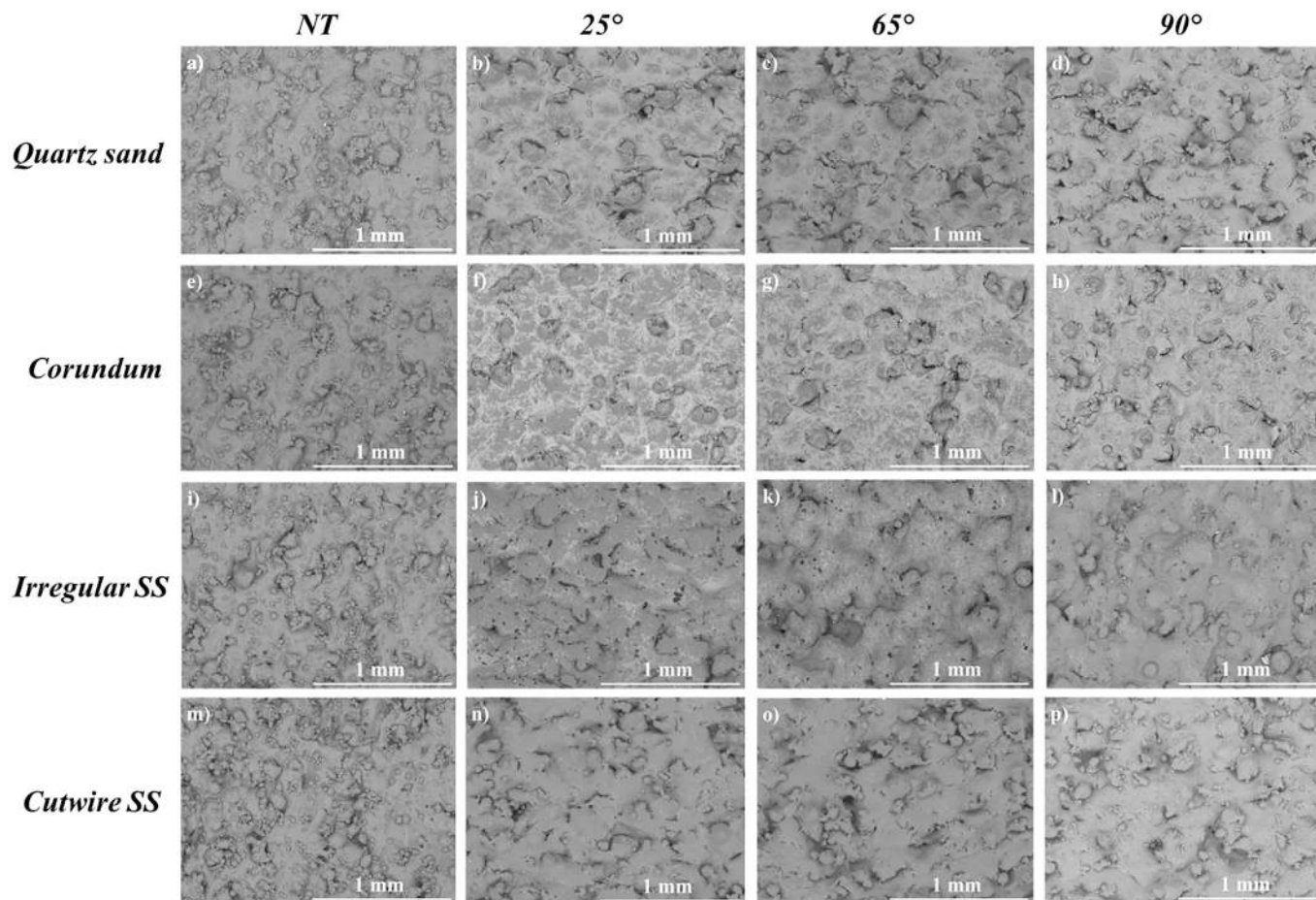

Fig. 7. SEM images of specimen surface before and after rotation-assisted FBF at $v = 1$ m/s.

sliding interaction associated with shear flow parallel to the specimen was established at low tilt angles. The 90° tilt angle, characterized by relative flow pattern orthogonal to the specimen, was the worst condition.

The surface roughness (S_a) decreased of about the 21% from its initial value for the best case (irregular SS, $\alpha = 25°$ or $65°$). The symmetry parameter S_{sk} changed notably toward a more pronounced asymmetry on the pits/valleys side (more negative values of S_{sk}). This result suggests that FBF promoted asperities removal more selectively than "filling" pits and valleys, regardless of the specific active surface modification phenomenon (plastic deformation, material removal or their combination). It is worth mentioning, however, that the assessment of S_{sk} might have been at least partly biased by an artifact, as the removal of sintered particles discloses underlying crater-like defects (darker areas on the surfaces reported in Fig. 7) that were originally formed due to non-optimal laser-matter interaction during L-PBF.

An appreciable reduction of P_{dq} is observed (Table 8). This finding, together with visual inspection of SEM images (Fig. 7), indicates that the evolution of the three surface morphology indicators is essentially dependent from the detachment of the sintered particles on the surface remaining after L-PBF. Fig. 7 highlights also that the samples treated with $\alpha = 25°$, regardless of the abrasive material used, presented the best surface quality improvement, although only the irregular and cutwire SS abrasives provided a substantial improvement.

Results obtained in experiments with rotational speed of 1 m/s are summarized in Fig. 8, reporting the finishing parameter, I_{fp} (Fig. 8a), and the wear (Fig. 8b) for the different bed materials. Plots in Fig. 8 indicate that: a) the SS abrasives yield the best finishing performance in terms of S_a reduction, the irregular SS material outperforming the regular one; b) the 25° and 65° tilt angles correspond to the best orientation of the specimen; c) surface modifications are dominated by removal of partly sintered powders attached to the surface, wear being largely correlated to I_{fp}.

3.2.2. Experiments with rotational speed $v = 2$ m/s

The surface texture parameters evolution is reported in Table 9 for the experiments with a rotational speed $v = 2$ m/s. Fig. 9 reports the SEM images of specimens before and after FBF. Surface modification induced at $v = 2$ m/s are more extensive than at $v = 1$ m/s, as expected. The influence of the nature of the abrasive material and of the tilt angle are largely preserved. The SS abrasives were more effective compared to quartz sand and corundum, the irregular SS particles slightly outperforming the regular ones. The tilt angles $\alpha = 25°$ and $65°$ provided the best finishing performance, inducing a remarkable surface roughness reduction of 67% and 57%, respectively. Analysis of the symmetry

parameter S_{sk} deserves consideration. For the irregular SS powder, S_{sk} decreased less for $\alpha = 25°$ than for $\alpha = 65°$ and $\alpha = 90°$, which is apparently at odds with the change of S_a for the same conditions. This result may be explained in the light of different surface mechanisms that may be at work in the best case compared with the other conditions. This result was confirmed by the SEM images reported in Fig. 9, which report a pronounced surface modification induced by the irregular SS at $\alpha = 25°$ (Fig. 9j). In the latter condition, not only the sintered powders were completely removed and the surface lying underneath exposed, but there is evidence of extensive material removal and plastic deformation. The appreciable contribution of the latter mechanism can be recognized by observing the directional texture of the resulting surface after the treatment and the presence of the brighter areas that could be associated to plastic strain (Fig. 9j). This phenomenon can be observed, with a decreasing intensity, also for the $\alpha = 65°$ (Fig. 9k) and $\alpha = 90°$ (Fig. 9l). On the other hand, the poor plastic deformation of the substrates treated with the cutwire SS abrasive justify the smaller reduction of roughness obtained for this material. For both the adopted v values, this result could be ascribed to the strongly reduced number of cutting edges of the cutwire geometry compared to the irregular one.

Fig. 10 illustrates the I_{fp} and wear for the experiments at $v = 2$ m/s. The effect of the tilt angle and abrasive material is confirmed as well as conditions corresponding to the best case i.e., irregular SS abrasive, $\alpha = 25°$. Again, the dominance of particle density over particle hardness as the key property of the abrasive material is confirmed.

3.2.3. Managing surface anisotropy and inhomogeneity

Experimental results give a clear indication of the superior performance of rotation-assisted FBF, of the greater relevance of particle density over particle hardness as the key property of the granular material, of the optimal pattern of the relative flow between the specimen and the fluidized granular solids, parallel shear flow being more effective than orthogonal or oblique flow.

Fig. 11 provides the starting point for addressing the issue of surface finishing anisotropy and inhomogeneity. Fig. 11a displays a pronounced anisotropy and inhomogeneity of a specimen machined at 2 m/s rotational speed, with irregular SS particles for 90 min. Table 10 reports the local surface morphology parameters measured at two selected zones (a and b in Fig. 11a) of area equal to 4×8 mm^2 each, taking the specimen center as reference point. Fig. 11b outlines the flow field of the fluidized granular solids near and past the specimen, which can be phenomenologically framed into an "oblique stagnation" flow pattern. It is remarkable that surface smoothing turns out to be less efficient close to the oblique stagnation point, and improves at specimen locations far from the point. This finding is consistent with the observation that
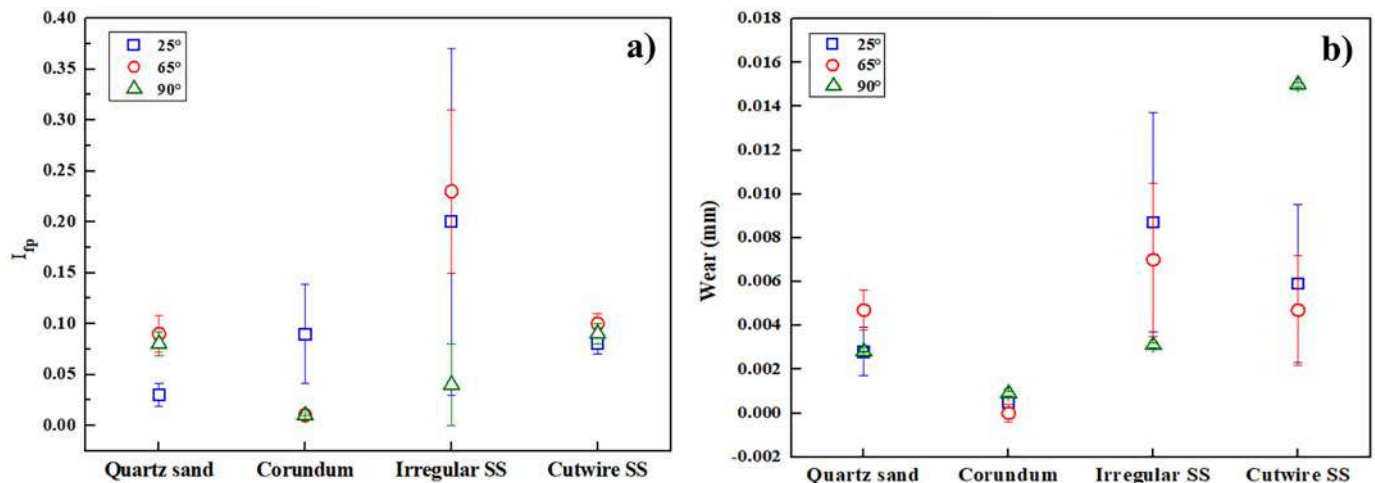

Fig. 8. Surface finishing parameter I_{fp} (a) and wear (b) for rotation-assisted FBF at $v = 1$ m/s (error bars indicate a deviation of $\pm\sigma$).

Table 9
Surface texture parameters of specimens for rotation-assisted FBF at $v = 2$ m/s (results are reported as mean $\pm$ σ).

|	Title angle α (°)	Quartz sand		Corundum		Irregular SS		Cutwire SS	
		NT	30 min	NT	30 min	NT	30 min	NT	30 min
S_a (μm)	25	22.9 ±0.6	20.8 ±0.9	19.6 ±0.3	19.8 ±0.2	21.7 ±1.1	7.2 ±0.2	25.1 ±1.1	14.1 ±4.5
	65	22.2 ±1.4	20 ±0.4	19.2 ±0.4	18.8 ±0.4	20.9 ±3.7	9 ±2.9	23.8 ±0.5	19 ±0.8
	90	23.1 ±2.4	21.3 ±2.8	18.7 ±0.7	18.3 ±0.6	19.7 ±0.6	11.9 ±0.4	23 ±0.8	20 ±0.2
S_{sk}	25	0.17 ±0.14	0.15 ±0.16	0.06 ±0.05	0.03 ±0.04	0.02 ±0	−0.89 ±0.04	0.22 ±0.16	−0.58 ±0.57
	65	0.04 ±0.01	0.01 ±0.00	−0.15 ±0.07	−0.35 ±0.07	−0.01 ±0.13	−1.94 ±0.34	0.11 ±0.08	−0.18 ±0.09
	90	0.16 ±0.14	0.28 ±0.21	−0.28 ±0.03	−0.28 ±0.04	−0.2 ±0.14	−1.66 ±0.2	0.05 ±0.04	−0.17 ±0.12
P_{dq} (°)	25	41 ±4.5	34 ±3.4	33 ±4.6	30 ±3.8	36 ±3.2	9 ±3.1	40 ±3.5	21 ±4.1
	65	42 ±3.4	31 ±2.4	35 ±3.9	30 ±3.7	36 ±2.6	8 ±2	42 ±2.6	28 ±2.1
	90	43 ±3.8	34 ±3.4	33 ±3.2	28 ±2.9	34 ±2.8	12 ±2.6	44 ±3.7	31 ±3
Weight loss (%)	25	–	0.1447 ± 0.1	–	0.1844 ± 0.05	–	5.26 ± 0.93	–	1.2638 ± 0.64
	65	–	0.3354 ± 0.05	–	0.0498 ± 0.01	–	1.3099 ± 0.5	–	0.5268 ± 0.3
	90	–	0.2415 ± 0.02	–	0.0000 ± 0.00	–	0.6888 ± 0.1	–	0.3780 ± 0.1
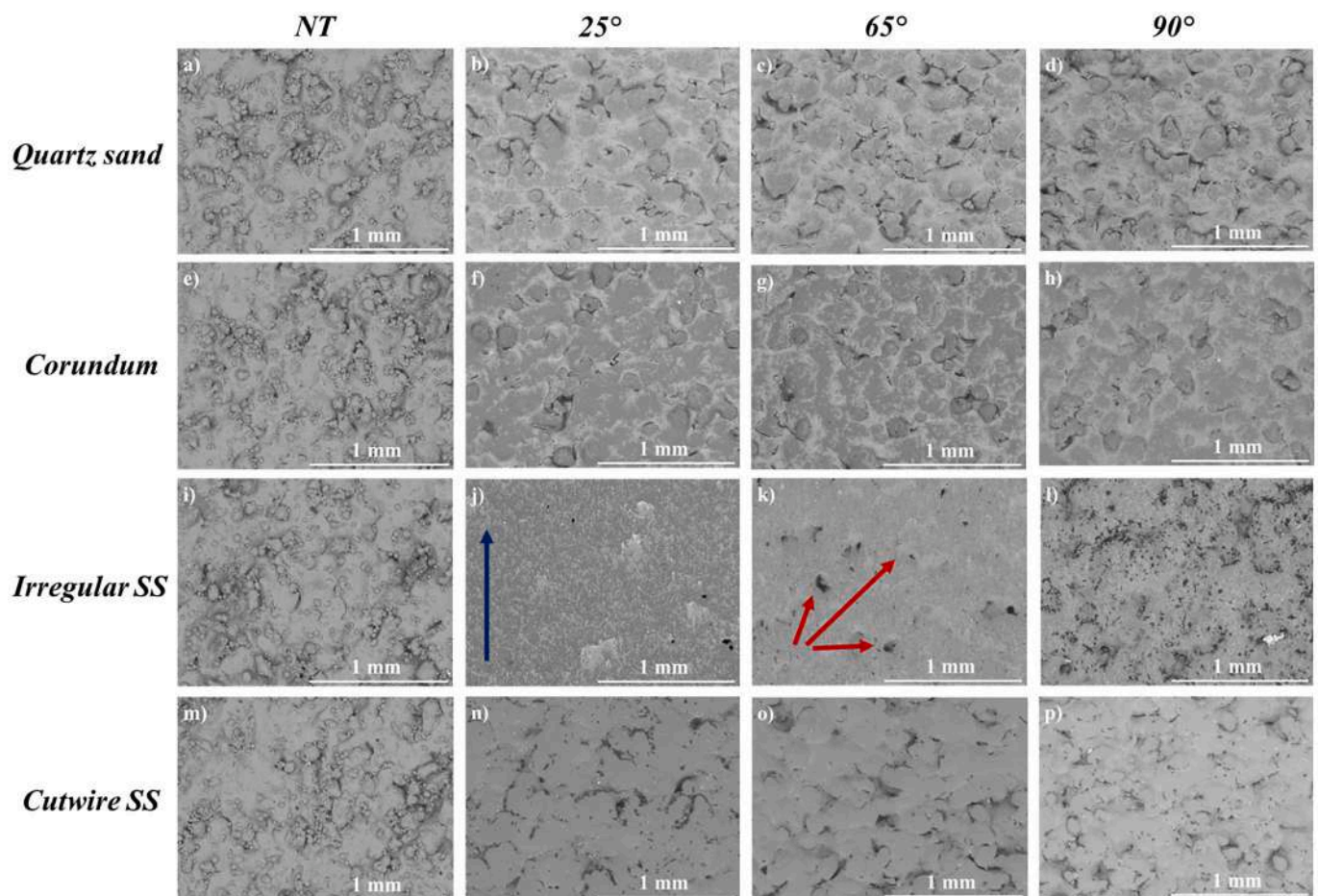
Fig. 9. SEM images of specimens surfaces before and after rotation-assisted FBF at $v = 2$ m/s. The blue arrow in inset j) indicates the directional smoothing pattern left from the abrasives, whereas the red arrows in inset k) highlight the intrinsic cavities of the L-PBF specimens that become more evident as the sintered powders are removed after FBF. (For interpretation of the references to colour in this figure legend, the reader is referred to the web version of this article.)
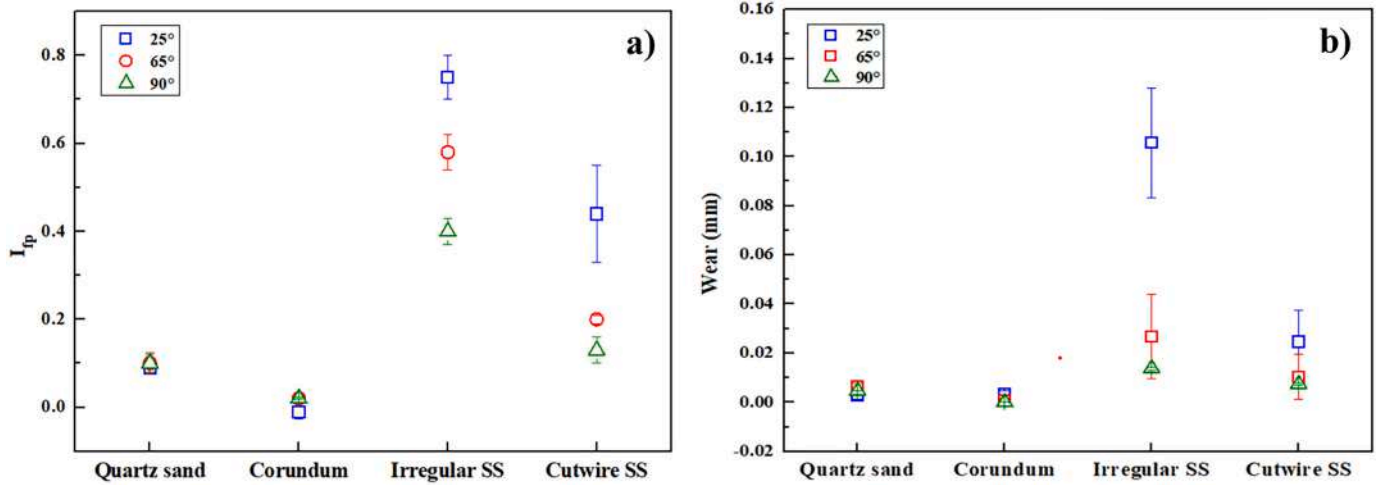
Fig. 10. Surface finishing parameter I_{fp} (a) and wear (b) for rotation-assisted FBF at $v = 2$ m/s (error bars indicate a deviation of $\pm\sigma$).
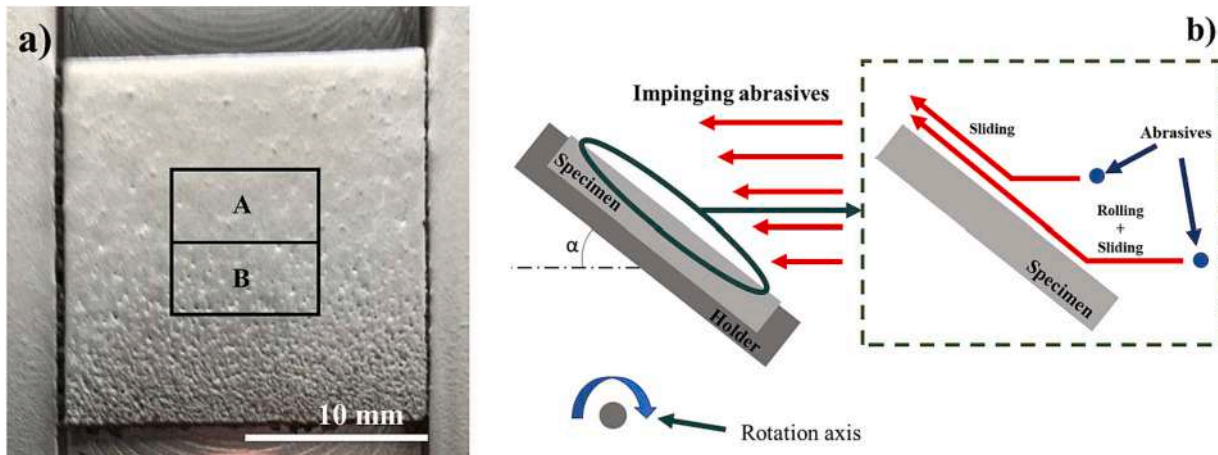

Fig. 11. a) Illustration of the induced surface anisotropy after the FBF best case conditions (a); b) Outline of the granular solids flow pattern close to and past the specimen.

Table 10
Surface texture parameters at selected measurement zones (see Fig. 11a) after rotation-assisted FBF at $v = 2$ m/s (results are reported as mean $\pm \sigma$).

Measurement zone	S_a (μm)	S_{sk}	P_{dq} (°)
A	6.2	−0.23	4.3 ± 0.2
B	7.3	−1.24	5.4 ± 0.1

Fig. 12. Images of specimens after alternated FBF treatments: a) Protocol I; b) Protocol II.

parallel shear flow is a more effective finishing mechanism than orthogonal flow. Close to the stagnation point particles exert more limited shear stress on the surface, hence smoothing ability, than at locations distant from the oblique stagnation point.

To overcome this limitation, two alternated FB finishing protocols were investigated starting from the best FBF conditions: I) after the single treatment step of 30 min, the sample was turned upside down and the treatment was repeated, resulting in a 1 h FBF treatment time; II) the 30 min of the single process step was split into 6 stages of 5 min each, and the specimen was turned upside down after each stage.

Fig. 12 reports the results of the two alternated FBF protocols. The surface morphological parameters and wear are reported in Table 11. The first notable outcome is that protocol I yields an apparently flatter surface, even if the final values of S_a are slightly higher compared to protocol II. This finding is consistent with analysis of the symmetry parameter S_{sk}, that was negligibly small after protocol I treatment,
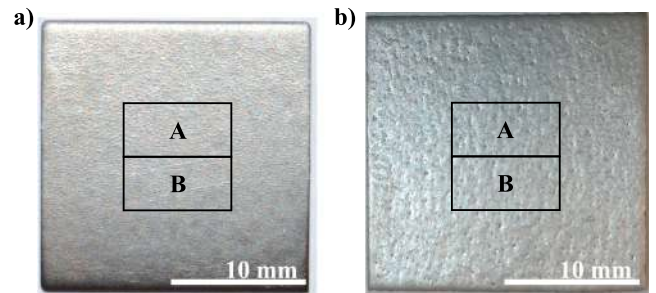
whereas it kept finite negative values after protocol II finishing. Protocol II produced the desired improvement of the surface homogeneity and a slight improvement of the overall roughness (S_a). This result could be justified by the following considerations: a) different treatment times experienced from the specimen could be the major source of the difference in the results; b) the more gradual surface modification induced by the protocol II might be the cause for the improved uniformity and roughness of the surface in comparison with the case I, for which the plastic deformation advancing fronts are also slightly visible in Fig. 12a.

Table 11

Surface texture parameters at selected measurement zones (see Fig. 11a) and wear after rotation-assisted FBF with alternated finishing protocols (results are reported as mean ± σ).

Experimental protocol	Measurement zone	S_a (μm)	S_{sk}	P_{dq} (°)	Wear (mm)
I	A	5.1	0.26	4.3 ± 0.2	0.19 ± 0.01
	B	6.3	0.48	5.4 ± 0.1	
II	A	4.9	−0.93	4.3 ± 0.2	0.09 ± 0.0155
	B	4.8	−0.81	4.9 ± 0.5	

Unfortunately, the same conclusion is not valid for the surface symmetry, as it probably requires a certain treatment time to be enhanced. In terms of wear, the protocol I led to greater material removal, as expected considering the longer treatment time, whereas slightly lower values were measured for the protocol II in comparison with the best case presented in Fig. 11.

Overall, a finishing strategy in rotation-assisted FBF improves the surface homogeneity and surface roughness, but further investigations are needed in order to assess the best conditions in terms of total process time and time-steps in order to perform a satisfactory surface finishing within reasonable a time span. On the other hand, it is worth to mention that the use of a FBF strategy further improved the smoothing efficiency, leading to a roughness reduction (S_a) of approximately the 75% and 77% for the strategies I and II respectively. Moreover, these values are appreciable and worthy of comparison in the overall scenario of surface polishing of AlSi10Mg alloy L-PBF specimens. For instance, very similar results were obtained in the case of chemical polishing and laser polishing of specimens of the same type and alloy, even for what concerns the starting surface roughness values, leading to percentage roughness reductions of about the 75% and 85% respectively [29,35]. However, a proper comparison is not possible in many other interesting cases, due to the different experimental conditions and, most of all, due to the differences in the surface characterization methodology. Examples of these cases are represented by the similar work carried out by Atzeni et al. concerning the FBF process [47] and the work of Nagalingam et al. concerning the hydrodynamic cavitation finishing of AlSi10Mg tubes produced through L-PBF [39]. In fact, despite the reported excellent results, these cannot be compared to the ones reported in the present study due to the measurement of R_a (mean roughness of the acquired profile) instead of S_a, being the former a result of a filtering process which is not applied generally for areal surface texture parameters.

4. Developing a mechanistic frame for surface FBF of metal objects

Modelling surface finishing of metal objects in fluidized beds should take into account the detailed micromechanics of the interaction between the object and the granular suspension. Much inspiration has been taken in the past from the neighboring field of erosion of objects immersed in fluidized beds. Finnie [65] pioneered these studies by deriving a single-particle erosive cutting model whence the material removal results from the cumulative action of individual particles and depends on impact velocity and angle and on the mechanical properties of the impinged material. Finnie's ductile erosion model has been successfully implemented into CFD-DEM [66] and DEM [67–69] simulations. Finnie's erosion model does not consider erosion by indirect impact and by sliding friction, hence it falls short for applications to dense particle systems.

Lyczkowski and Bouillard [70] comprehensively reviewed erosion models proposed in the literature which they categorized into single-particle models, dense phase fluidized bed models and power/energy dissipation models. Single-particle and dense phase models were developed considering the interaction of a single particle and many particles with a planar wall, respectively. The finishing process can occur under purely ductile mode, purely brittle mode or failure-fatigue mode [70,71]. Energy dissipation models express erosion rates on the basis of the deformation work, lumping ductile, brittle, abrasive and impact erosion together. They developed an energy dissipation model for the calculation of the average erosion rate in fluidized beds [70,72], based on a simplified closed form of the monolayer kinetic energy dissipation model (SCFMED) for erosion of tubes in fluidized beds.

A critical analysis of the phenomenology of FBF suggests that there is a fundamental argument that may jeopardize extension of mathematical and phenomenological models borrowed from the field of erosion of objects and internals in fluidized beds to the field of surface FBF. In fact, erosion of objects in fluidized beds is a case where initially smooth surfaces are exposed to the damage and wear from fluidized particles. The hardness of the abrasive material plays a crucial role in erosion, as it represents the ability of the particles to cause early indentations and defects in an otherwise smooth surface whence further wear and material loss may originate. On the contrary, FBF entails smoothing out of a surface which is already inherently rough and indented under the polishing action of the fluidized suspension. Results reported in Section 3 highlighted that the reduction of the mean surface roughness S_a during FBF occurred together with a reduction of the skewness parameter S_{sk}. This implies that surface finishing is mainly due to the removal of the protuberances and peaks by interaction with the fluidized bed.

In dense fluidized beds, solids motion takes place as a coherent granular flow, with multiple contact points between particles, enduring force chains, and momentum exchange between the fluidized particles and immersed surfaces taking place essentially through shear forces rather than impact. The relative velocity between the fluidized bed and the specimen is small when compared with particle impact velocities that would be required to induce plastic deformation and material loss. This is even more so in the proximity of the surface, where large solids concentration and the presence of asperities on the specimen promote no-slip flow patterns. An outline of the likely interactive pattern between the granular shear flow and an asperity is reported in Fig. 13.

Under these conditions, the shear stress exerted by the fluidized solids on the specimen surface may be well approximated by the Bagnold Eq. [73]:

$$\tau = \mu(\phi_s)\rho_s d_p^2 \bullet \dot{\gamma}^2 \tag{1}$$

where τ is the shear stress, μ is a dimensionless function dependent on solids concentration ϕ_s, ρ_s the density of the abrasive solids, d_p the abrasive solids diameter and $\dot{\gamma}$ the shear rate. In this frame, a corrugated
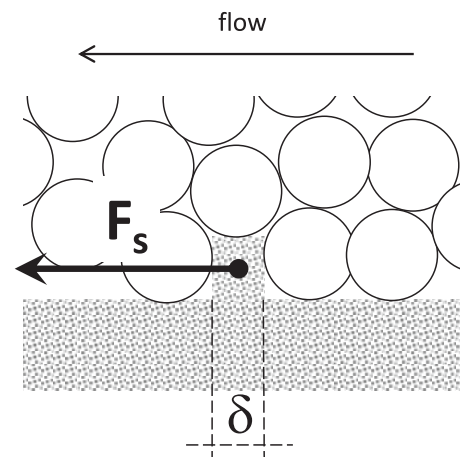

Fig. 13. Schematic representation of shear flow past the specimen and force acting on asperities.

surface is finished by the removal of asperities in a fluidized bed if the shear forces overtake the shear resistance of the asperity, by either plastic or brittle failure.

The detachment of the asperity occurs when:

$$F_s = \tau \bullet \delta^2 = \mu(\phi_s)\rho_s d_p^2 \bullet \dot\gamma^2 \bullet \delta^2 > F_{r,lim} = \tau_{r,lim} \bullet \delta^2 \tag{2}$$

where F_s represents the shear force exerted by the fluidized medium on the asperity, δ is the characteristic contact length of the asperity and $F_{r,lim}$ and $\tau_{r,lim}$ are the limit values of the resistant force and shear stress on the verge of the failure of the asperity, respectively. By the following approximation:

$$d_p^2 \bullet \dot\gamma^2 \approx v^2 \tag{3}$$

it is possible to derive a finishing criterion:

$$\mu \bullet \rho_s v^2 > \tau_{r,lim} \tag{4}$$

where v is the relative velocity between the specimen and the fluidized medium.

This criterion indicates that the finishing efficiency scales as the product $\rho_s v^2$. Accordingly, the effectiveness of the finishing process scales linearly with the granular medium density ρ_s. The particle hardness does not play a role in the proposed framework. Surface finishing is strongly (quadratically) enhanced as the relative velocity between the specimen and the fluidized suspension is increased.

It is remarkable that all the trends predicted by the proposed model as regards the influence of operational parameters of FBF are fully consistent with the experimental findings. This is encouraging in view of the perspective to develop phenomenological and mathematical models of surface finishing that are specific to FBF, rather than borrowed from the field of erosion of objects in fluidized beds.

5. Conclusions

Fluidized Bed Finishing (FBF) of specimens manufactured by the Laser-Powder Bed Fusion (L-PBF) AM technology has been investigated under a variety of operating conditions. Two variants of FBF have been tested, the first consisting of the finishing of a stationary specimen immersed in the bed, the second based on the establishment of relative rotational motion between the immersed specimen and the fluidized bed. The effectiveness of FBF has been assessed, for both stationary and rotation-assisted variants, as a function of the nature of the abrasive material, of the tilt angle of the specimen with respect to the prevailing motion of the fluidized particles, and of the finishing time. The influence of the rotational speed was also assessed for rotation-assisted FBF.

Key findings of the study are hereby summarized.

- Rotation-assisted FBF is far more efficient than stationary FBF, and surface finishing increases as the rotational speed increases. A maximum reduction of the areal mean surface roughness S_a by about the 67% was obtained under rotation-assisted conditions, with final values of about 7.2 ± 0.2 μm. The reduction did not exceed 10% under stationary FBF conditions.
- The surface finishing efficiency depends on the nature and properties of the abrasive bed material. Experimental results provide unequivocal evidence that particle density, rather than particle hardness, is the key to the abrasive potential of powders in FBF conditions. The best performances were obtained with the use of irregular steel particles. Of course, the use of bed materials characterized by high density can imply higher fluidization gas flow rates and thus higher operation costs.
- Surface finishing depends on the orientation of the specimen with respect to the prevailing flow of the fluidized particles. Surface finishing is maximized when plain shear flow of fluidized particles is

established close to and past the specimen, compared to orthogonal or oblique shear flow.
- The prevailing finishing mechanism is associated with the removal from the surface of partly sintered particles, left behind as a consequence of balling during the AM stage. In the best case conditions, complete removal of the sintered powders on the sample surface due to balling was achieved, as well as modification of the surface lying underneath due to both material removal and plastic deformation. The concurrence of particle removal and plastic deformation explains the fact that surface finishing may only partly be correlated with surface wear and fractional loss of material upon finishing.
- Anisotropy and inhomogeneity in surface finishing may be managed by applying protocols based on multiple finishing cycles with alternated flow of the fluidized particles past the specimen. In the present study, the best results were obtained by splitting a 30 min FBF overall processing time into 5 min stages, with flow inversion at each stage. A homogeneously finished surface was obtained, with a final surface roughness of about 4.8 μm.
- Extrapolation of models developed for erosion of objects and internals in fluidized beds to FBF may lead to inaccurate predictions, due to critical differences as regards the initial morphology of the surface and the micromechanics of powder-specimen interaction. Instead, a simple phenomenological model based on a failure criterion of a single protuberance and on Bagnold's equation to express the shear stress exerted by plain shear flow of a granular system past the surface has the ability to reproduce the key findings of the study.

Altogether, results of the present study provide an additional basis to assess the potential of the FBF technology and lay the path for further improvements.

CRediT authorship contribution statement

Maurizio Troiano: Conceptualization, Methodology, Formal analysis, Investigation, Writing – original draft. **Andrea El Hassanin:** Conceptualization, Methodology, Formal analysis, Investigation, Writing – original draft. **Roberto Solimene:** Conceptualization, Methodology, Supervision, Writing – review & editing. **Alessia Teresa Silvestri:** Investigation, Visualization. **Fabrizio Scala:** Conceptualization. **Antonino Squillace:** Conceptualization, Methodology, Supervision. **Piero Salatino:** Conceptualization, Methodology, Supervision, Writing – review & editing.

Declaration of Competing Interest

The authors declare that they have no known competing financial interests or personal relationships that could have appeared to influence the work reported in this paper.

Data availability

Data will be made available on request.

Acknowledgements

References

[1] J. Li, C. Myant, B. Wu, The Current Landscape for Additive Manufacturing Research, Imperial College London Additive Manufacturing Network, 2016, https://doi.org/10.25561/39726.

[2] O. Diegel, A. Nordin, D. Motte, Additive manufacturing technologies, in: O. Diegel, A. Nordin, D. Motte (Eds.), A Practical Guide to Design for Additive Manufacturing, Springer Singapore, Singapore, 2019, pp. 19–39, https://doi.org/10.1007/978-981-13-8281-9_2.

[3] S.A.M. Tofail, E.P. Koumoulos, A. Bandyopadhyay, S. Bose, L. O'Donoghue, C. Charitidis, Additive manufacturing: scientific and technological challenges, market uptake and opportunities, Mater. Today 21 (2018) 22–37, https://doi.org/10.1016/j.mattod.2017.07.001.

[4] S. Ford, M. Despeisse, Additive manufacturing and sustainability: an exploratory study of the advantages and challenges, J. Clean. Prod. 137 (2016) 1573–1587, https://doi.org/10.1016/j.jclepro.2016.04.150.

[5] D. Herzog, V. Seyda, E. Wycisk, C. Emmelmann, Additive manufacturing of metals, Acta Mater. 117 (2016) 371–392, https://doi.org/10.1016/j.actamat.2016.07.019.

[6] W.E. Frazier, Metal additive manufacturing: a review, J. Mater. Eng. Perform. 23 (2014) 1917–1928, https://doi.org/10.1007/s11665-014-0958-z.

[7] V. Lampitella, M. Trofa, A. Astarita, G. D'Avino, Discrete element method analysis of the spreading mechanism and its influence on powder bed characteristics in additive manufacturing, Micromachines (Basel). 12 (2021) 392, https://doi.org/10.3390/mi12040392.

[8] D. Sofia, D. Macrì, D. Barletta, P. Lettieri, M. Poletto, Use of titania powders in the laser sintering process: link between process conditions and product mechanical properties, Powder Technol. 381 (2021) 181–188, https://doi.org/10.1016/j.powtec.2020.11.075.

[9] W. Nan, M. Pasha, T. Bonakdar, A. Lopez, U. Zafar, S. Nadimi, M. Ghadiri, Jamming during particle spreading in additive manufacturing, Powder Technol. 338 (2018) 253–262, https://doi.org/10.1016/j.powtec.2018.07.030.

[10] W. Nan, M. Ghadiri, Numerical simulation of powder flow during spreading in additive manufacturing, Powder Technol. 342 (2019) 801–807, https://doi.org/10.1016/j.powtec.2018.10.056.

[11] M. Ahmed, M. Pasha, W. Nan, M. Ghadiri, A simple method for assessing powder spreadability for additive manufacturing, Powder Technol. 367 (2020) 671–679, https://doi.org/10.1016/j.powtec.2020.04.033.

[12] H. Masuo, Y. Tanaka, S. Morokoshi, H. Yagura, T. Uchida, Y. Yamamoto, Y. Murakami, Influence of defects, surface roughness and HIP on the fatigue strength of Ti-6Al-4V manufactured by additive manufacturing, Int. J. Fatigue 117 (2018) 163–179, https://doi.org/10.1016/j.ijfatigue.2018.07.020.

[13] A. El Hassanin, F. Scherillo, A.T. Silvestri, A. Caraviello, R. Sansone, A. Astarita, A. Squillace, Heat Treatment of Inconel Selective Laser Melted Parts: Microstructure Evolution, AIP Conf Proc, American Institute of Physics Inc., 2019, https://doi.org/10.1063/1.5112599.

[14] N. Sanaei, A. Fatemi, Analysis of the effect of surface roughness on fatigue performance of powder bed fusion additive manufactured metals, Theor. Appl. Fract. Mech. 108 (2020), 102638, https://doi.org/10.1016/j.tafmec.2020.102638.

[15] G. Strano, L. Hao, R.M. Everson, K.E. Evans, Surface roughness analysis, modelling and prediction in selective laser melting, J. Mater. Process. Technol. 213 (2013) 589–597, https://doi.org/10.1016/j.jmatprotec.2012.11.011.

[16] T. DebRoy, H.L. Wei, J.S. Zuback, T. Mukherjee, J.W. Elmer, J.O. Milewski, A. M. Beese, A. Wilson-Heid, A. De, W. Zhang, Additive manufacturing of metallic components – process, structure and properties, Prog. Mater. Sci. 92 (2018) 112–224, https://doi.org/10.1016/j.pmatsci.2017.10.001.

[17] B. Soundararajan, D. Sofia, D. Barletta, M. Poletto, Review on modeling techniques for powder bed fusion processes based on physical principles, Addit. Manuf. 47 (2021), 102336, https://doi.org/10.1016/j.addma.2021.102336.

[18] J.Y. Lee, A.P. Nagalingam, S.H. Yeo, A review on the state-of-the-art of surface finishing processes and related ISO/ASTM standards for metal additive manufactured components, Virtual Phys. Prototyp. 16 (2021) 68–96, https://doi.org/10.1080/17452759.2020.1830346.

[19] J. Boban, A. Ahmed, E.K. Jithinraj, M.A. Rahman, M. Rahman, Polishing of additive manufactured metallic components: retrospect on existing methods and future prospects, Int. J. Adv. Manuf. Technol. 121 (2022) 83–125, https://doi.org/10.1007/s00170-022-09382-y.

[20] M.A. Bernevig-Sava, C. Stamate, N.M. Lohan, A.M. Baciu, I. Postolache, C. Baciu, E. R. Baciu, Considerations on the surface roughness of SLM processed metal parts and the effects of subsequent sandblasting, IOP Conf. Ser. Mater. Sci. Eng. 572 (2019), https://doi.org/10.1088/1757-899X/572/1/012071.

[21] J. Gumpinger, A.D. Brandao, E. Beevers, T. Rohr, T. Ghidini, S. Beretta, S. Romano, Expression of additive manufacturing surface irregularities through a flaw-based assessment, in: Structural Integrity of Additive Manufactured Parts, 2020, pp. 234–239, https://doi.org/10.1520/STP162020180098.

[22] B. AlMangour, J.M. Yang, Improving the surface quality and mechanical properties by shot-peening of 17-4 stainless steel fabricated by additive manufacturing, Mater. Des. 110 (2016) 914–924, https://doi.org/10.1016/j.matdes.2016.08.037.

[23] A. Maamoun, M. Elbestawi, S. Veldhuis, Influence of shot peening on AlSi10Mg parts fabricated by additive manufacturing, J. Manuf. Mater. Proc. 2 (2018) 40, https://doi.org/10.3390/jmmp2030040.

[24] J.M. Flynn, A. Shokrani, S.T. Newman, V. Dhokia, Hybrid additive and subtractive machine tools - research and industrial developments, Int. J. Mach. Tools Manuf. 101 (2016) 79–101, https://doi.org/10.1016/j.ijmachtools.2015.11.007.

[25] Y. Kaynak, O. Kitay, The effect of post-processing operations on surface characteristics of 316L stainless steel produced by selective laser melting, Addit. Manuf. 26 (2019) 84–93, https://doi.org/10.1016/j.addma.2019.01.012.

[26] C. Bouland, V. Urlea, K. Beaubier, M. Samoilenko, V. Brailovski, Abrasive flow machining of laser powder bed-fused parts: numerical modeling and experimental validation, J. Mater. Process. Technol. 273 (2019), 116262, https://doi.org/10.1016/j.jmatprotec.2019.116262.

[27] U.S. Kim, J.W. Park, High-quality surface finishing of industrial three-dimensional metal additive manufacturing using electrochemical polishing, Int. J. Precision Eng. Manufact. Green Technol. 6 (2019) 11–21, https://doi.org/10.1007/s40684-019-00019-2.

[28] E. Lyczkowska, P. Szymczyk, B. Dybała, E. Chlebus, Chemical polishing of scaffolds made of Ti-6Al-7Nb alloy by additive manufacturing, Archives of Civil and Mechanical Engineering. 14 (2014) 586–594, https://doi.org/10.1016/j.acme.2014.03.001.

[29] F. Scherillo, Chemical surface finishing of AlSi10Mg components made by additive manufacturing, Manuf. Lett. 19 (2019) 5–9, https://doi.org/10.1016/j.mfglet.2018.12.002.

[30] F. Scherillo, E. Manco, A. El Hassanin, S. Franchitti, C. Pirozzi, R. Borrelli, Chemical surface finishing of electron beam melted Ti6Al4V using HF-HNO3 solutions, J. Manuf. Process. 60 (2020) 400–409, https://doi.org/10.1016/j.jmapro.2020.10.033.

[31] K. Wissenbach, Surface treatment, in: R. Poprawe (Ed.), Tailored Light 2: Laser Application Technology, Springer Berlin Heidelberg, Berlin, Heidelberg, 2011, pp. 173–239, https://doi.org/10.1007/978-3-642-01237-2_11.

[32] B. Liu, B.Q. Li, Z. Li, Selective laser remelting of an additive layer manufacturing process on AlSi10Mg, Results Phys. 12 (2019) 982–988, https://doi.org/10.1016/j.rinp.2018.12.018.

[33] Q. Han, Y. Jiao, Effect of heat treatment and laser surface remelting on AlSi10Mg alloy fabricated by selective laser melting, Int. J. Adv. Manuf. Technol. 102 (2019) 3315–3324, https://doi.org/10.1007/s00170-018-03272-y.

[34] J. Li, D. Zuo, Laser polishing of additive manufactured Ti6Al4V alloy: a review, Opt. Eng. 60 (2021) 1–16, https://doi.org/10.1117/1.oe.60.2.020901.

[35] A. El Hassanin, M.A. Obeidi, F. Scherillo, D. Brabazon, CO2 laser polishing of laser-powder bed fusion produced AlSi10Mg parts, Surf. Coat. Technol. 419 (2021), 127291, https://doi.org/10.1016/j.surfcoat.2021.127291.

[36] M.A. Obeidi, E. Mccarthy, I.U. Ahad, Laser polishing of Additive Manufactured 316L SST Cylindrical Samples, 2023.

[37] V.K. Jain, S.G. Adsul, Experimental investigations into abrasive flow machining (AFM), Int. J. Mach. Tools Manuf. 40 (2000) 1003–1021, https://doi.org/10.1016/S0890-6955(99)00114-5.

[38] H. Yamaguchi, O. Fergani, P.Y. Wu, Modification using magnetic field-assisted finishing of the surface roughness and residual stress of additively manufactured components, CIRP Ann. Manuf. Technol. 66 (2017) 305–308, https://doi.org/10.1016/j.cirp.2017.04.084.

[39] A.P. Nagalingam, H.K. Yuvaraj, S.H. Yeo, Synergistic effects in hydrodynamic cavitation abrasive finishing for internal surface-finish enhancement of additive-manufactured components, Addit. Manuf. 33 (2020), 101110, https://doi.org/10.1016/j.addma.2020.101110.

[40] J.G. Yates, P. Lettieri, Fluidized-bed Reactors: Processes and Operating Conditions, Springer, 2016, https://doi.org/10.1007/978-3-319-39593-7.

[41] M. Barletta, A new technology in surface finishing: fluidized bed machining (FBM) of aluminium alloys, J. Mater. Process. Technol. 173 (2006) 157–165, https://doi.org/10.1016/j.jmatprotec.2005.11.020.

[42] M. Barletta, S. Guarino, G. Rubino, V. Tagliaferri, Progress in fluidized bed assisted abrasive jet machining (FB-AJM): internal polishing of aluminium tubes, Int. J. Mach. Tools Manuf. 47 (2007) 483–495, https://doi.org/10.1016/j.ijmachtools.2006.06.005.

[43] M. Barletta, D. Ceccarelli, S. Guarino, V. Tagliaferri, Fluidized bed assisted abrasive jet machining (FB-AJM): precision internal finishing of Inconel 718 components, J. Manuf. Sci. E. T. ASME 129 (2007) 1045–1059, https://doi.org/10.1115/1.2752831.

[44] M. Barletta, Progress in abrasive fluidized bed machining, J. Mater. Process. Technol. 209 (2009) 6087–6102, https://doi.org/10.1016/j.jmatprotec.2009.04.009.

[45] M. Barletta, V. Tagliaferri, F. Trovalusci, F. Veniali, A. Gisario, The mechanisms of material removal in the fluidized bed machining of polyvinyl chloride substrates, J. Manuf. Sci. E. T. ASME 135 (2013) 1–11, https://doi.org/10.1115/1.4007956.

[46] M. Barletta, F. Pietrobono, G. Rubino, V. Tagliaferri, Drag finishing of sensitive workpieces with fluidized abrasives, J. Manuf. Process. 16 (2014) 494–502, https://doi.org/10.1016/j.jmapro.2014.06.003.

[47] E. Atzeni, M. Barletta, F. Calignano, L. Iuliano, G. Rubino, V. Tagliaferri, Abrasive fluidized bed (AFB) finishing of AlSi10Mg substrates manufactured by direct metal laser sintering (DMLS), Addit. Manuf. 10 (2016) 15–23, https://doi.org/10.1016/j.addma.2016.01.005.

[48] E. Atzeni, G. Rubino, A. Salmi, F. Trovalusci, Abrasive fluidized bed finishing to improve the fatigue behaviour of Ti6Al4V parts fabricated by electron beam melting, Int. J. Adv. Manuf. Technol. 110 (2020) 557–567, https://doi.org/10.1007/s00170-020-05814-9/Published.

[49] E. Atzeni, S. Genna, E. Menna, G. Rubino, A. Salmi, F. Trovalusci, Surface finishing of additive manufactured ti-6al-4v alloy: a comparison between abrasive fluidized bed and laser finishing, Materials. 14 (2021), https://doi.org/10.3390/ma14185366.

[50] E. Atzeni, S. Genna, A. Salmi, F. Trovalusci, G. Rubino, Abrasive fluidized bed finishing of additive manufactured cobalt-chrome parts: effects on surface morphology and fatigue behavior, Int. J. Adv. Manuf. Technol. 124 (2023) 1939–1949, https://doi.org/10.1007/s00170-022-10580-x.

[51] T. Kim, H. Lee, Simulation and experimental analysis of abrasive fluidized bed machining process, J. Mech. Sci. Technol. 34 (2020) 2153–2160, https://doi.org/10.1007/s12206-020-0436-5.

[52] A. El Hassanin, M. Troiano, A.T. Silvestri, V. Contaldi, F. Scherillo, R. Solimene, F. Scala, A. Squillace, P. Salatino, Fluidised bed machining of metal additive

manufactured parts, AIP Conf. Proc. 2113 (2019), https://doi.org/10.1063/1.5112685.

[53] A. El Hassanin, M. Troiano, A.T. Silvestri, V. Contaldi, F. Scherillo, R. Solimene, F. Scala, A. Squillace, P. Salatino, Influence of abrasive materials in fluidised bed machining of AlSi10Mg parts made through selective laser melting technology, Key Eng. Mater. 813 KEM (2019) 129–134, https://doi.org/10.4028/www.scientific.net/KEM.813.129.

[54] M. Troiano, A. El Hassanin, A.T. Silvestri, F. Scherillo, F. Scala, R. Solimene, A. Squillace, P. Salatino, Fluidized bed machining of metal objects produced by additive manufacturing, in: CFB 2021 - Proceedings of the 13th International Conference on Fluidized Bed Technology, 2021, pp. 623–628. https://www.scopus.com/inward/record.uri?eid=2-s2.0-85110901477&partnerID=40&md5=3439de8abbc2c2017b642c0a4b3f59e2.

[55] A. El Hassanin, M. Troiano, F. Scherillo, A.T. Silvestri, V. Contaldi, R. Solimene, F. Scala, A. Squillace, P. Salatino, Rotation-assisted abrasive fluidised bed machining of alsi10mg parts made through selective laser melting technology, Procedia Manuf. 47 (2020) 1043–1049, https://doi.org/10.1016/j.promfg.2020.04.113.

[56] T. Kim, H. Lee, Preliminary study on fluidized bed chemical mechanical polishing (FB-CMP) process for stainless steel 304 (SS304), Micromachines (Basel). 11 (2020) 705, https://doi.org/10.3390/mi11070705.

[57] ASTM International, Standard test method for particle size distribution of metal powders and related compounds by light scattering 1 (97) (2001) 1–5, https://doi.org/10.1520/B0822-20.

[58] D. Beckers, N. Ellendt, U. Fritsching, V. Uhlenwinkel, Impact of process flow conditions on particle morphology in metal powder production via gas atomization, Adv. Powder Technol. 31 (2020) 300–311, https://doi.org/10.1016/j.apt.2019.10.022.

[59] D. Kunii, O. Levenspiel, CHAPTER 13 - heat transfer between fluidized beds and surfaces, in: D. Kunii, O. Levenspiel (Eds.), Fluidization Engineering, Second edition, Butterworth-Heinemann, Boston, 1991, pp. 313–336, https://doi.org/10.1016/B978-0-08-050664-7.50019-6.

[60] ISO 25178-2:2012, Standards Publication Geometrical Product Specifications (GPS) — Surface Texture: Areal - Part 2: Terms, Definitions and Surface Parameters, 2012.

[61] BS EN ISO 4287, Geometrical Product Specifications (GPS) — Surface Texture: Profile Method: Terms, Definitions and Surface Texture Parameters, British Standards Institution, 1998.

[62] M. Yonehara, T. Matsui, K. Kihara, H. Isono, A. Kijima, T. Sugibayashi, Evaluation method of surface texture by surface roughness based on geometrical product specifications (GPS), Mater. Trans. 45 (2004) 1019–1026, https://doi.org/10.2320/matertrans.45.1019.

[63] C.S. Campbell, Stress-controlled elastic granular shear flows, J. Fluid Mech. 539 (2005) 273–297, https://doi.org/10.1017/S0022112005005616.

[64] C.S. Campbell, Granular material flows - an overview, Powder Technol. 162 (2006) 208–229, https://doi.org/10.1016/j.powtec.2005.12.008.

[65] I. Finnie, Erosion of surfaces by solid particles, Wear. 3 (1960) 87–103, https://doi.org/10.1016/0043-1648(60)90055-7.

[66] K.W. Chu, S.B. Kuang, A.B. Yu, A. Vince, G.D. Barnett, P.J. Barnett, Prediction of wear and its effect on the multiphase flow and separation performance of dense medium cyclone, Miner. Eng. 56 (2014) 91–101, https://doi.org/10.1016/j.mineng.2013.10.029.

[67] H. Ashrafizadeh, F. Ashrafizadeh, A numerical 3D simulation for prediction of wear caused by solid particle impact, Wear. 276–277 (2012) 75–84, https://doi.org/10.1016/j.wear.2011.12.003.

[68] L. Xu, Q. Zhang, J. Zheng, Y. Zhao, Numerical prediction of erosion in elbow based on CFD-DEM simulation, Powder Technol. 302 (2016) 236–246, https://doi.org/10.1016/j.powtec.2016.08.050.

[69] Y. Zhao, L. Xu, J. Zheng, CFD–DEM simulation of tube erosion in a fluidized bed, AICHE J. 63 (2017) 418–437, https://doi.org/10.1002/aic.15398.

[70] R.W. Lyczkowski, J.X. Bouillard, State-of-the-art review of erosion modeling in fluid/solids systems, Prog. Energy Combust. Sci. 28 (2002) 543–602, https://doi.org/10.1016/S0360-1285(02)00022-9.

[71] M. Ghadiri, Z. Zhang, Impact attrition of particulate solids. Part 1: A theoretical model of chipping, Chem. Eng. Sci. 57 (2002) 3659–3669, https://doi.org/10.1016/S0009-2509(02)00240-3.

[72] R.W. Lyczkowski, J.X. Bouillard, Scaling and guidelines for erosion in fluidized beds, Powder Technol. 125 (2002) 217–225, https://doi.org/10.1016/S0032-5910(01)00509-5.

[73] R.A. Bagnold, Experiments on a gravity-free dispersion of large solid spheres in a Newtonian fluid under shear, Proc. R. Soc. Lond. A Math. Phys. Sci. 225 (1954) 49–63, https://doi.org/10.1098/rspa.1954.0186.